Design of Robust MPPT Controller for Grid-connected PMSG-Based Wind Turbine via Perturbation Observation Based Nonlinear Adaptive Control

Jian Chen[a], Wei Yao[b,*], Chuan-Ke Zhang[c], Yaxing Ren[d], Lin Jiang[d]

[a] *School of Electrical Engineering, Yancheng Institute of Technology, Yancheng, 224051, China*
[b] *State Key Laboratory of Advanced Electromagnetic Engineering and Technology, School of Electrical and Electronics Engineering, Huazhong University of Science and Technology, Wuhan, 430074, China*
[c] *School of Automation, China University of Geosciences, Wuhan, 430074, China*
[d] *Department of Electrical Engineering and Electronics, University of Liverpool, Liverpool, L69 3GJ, United Kingdom.*

Abstract

This paper presents a robust maximum power point tracking (MPPT) control scheme for a grid-connected permanent magnet synchronous generator based wind turbine (PMSG-WT) using perturbation observation based nonlinear adaptive control. In the proposed control scheme, system nonlinearities, parameter uncertainties, and external disturbances of the PMSG-WT are represented as a lumped perturbation term, which is estimated by a high-gain perturbation observer. The estimate of the lumped perturbation is employed to compensate the actual perturbation and further achieve adaptive feedback linearizing control of the original nonlinear system, without requiring the detailed system model and full state measurements. The effectiveness of the proposed control scheme is verified through both simulation studies and experimental tests. The results show that, compared with the conventional vector controller and the standard feedback linearizing controller, the proposed control strategy provides higher power conversion efficiency and has better dynamic performances and robustness against parameter uncertainties and external disturbances.

Keywords: Permanent magnet synchronous generator (PMSG), nonlinear adaptive control (NAC), maximum power point tracking (MPPT), perturbation observer, perturbation estimation.

1. Introduction

Wind energy has become an attractive and competitive clean renewable source. Most current wind energy conversion systems (WECSs) employ variable speed wind turbines such as doubly-fed induction generator (DFIG) based wind turbine and permanent magnet synchronous generator (PMSG) based wind turbine [1]-[8]. A DFIG-based wind turbine normally uses a gearbox to couple the rotor shaft of the wind turbine and the DFIG, which increases the

*Corresponding Author: W. Yao, Tel.: +86 13657247542, Email: w.yao@hust.edu.cn

maintenance cost and failure rate of the whole wind energy conversion system (WECS) [9]. Since the rotor of the PMSG can be coupled directly to the one of the wind turbine, the usage of the gearbox is removed, and the installment of direct-drive PMSG-based wind turbine (PMSG-WT) nowadays has been increasing, especially in offshore wind farms, together with other merits such as high efficiency and high torque to weight ratio [10]-[17].

A maximum power point tracking (MPPT) control scheme can increase the power conversion efficiency by regulating the mechanical rotation speed according to actual wind speeds [18, 19, 20]. Therefore, to improve the overall efficiency of a WECS, an effective MPPT control scheme is essential [21, 22, 23, 24]. To extract maximum power from time-varying wind power, some typical controllers are proposed and designed based on an approximated linear model and linear techniques, such as conventional vector control (VC) with proportional-integral (PI) loops [14, 25] and linear quadratic Gaussian [26]. Among these control strategies, the VC is the current industrial standard solution. Despite the advantages of simplicity and decoupling control of active and reactive power, the VC based MPPT (VC-MPPT) may not provide satisfactory performance as the PMSG-WT is a highly nonlinear system, which operates at time-varying and wide-range operation points, due to time-varying wind speed. Therefore, the VC-MPPT designed and tuned based on one operation point is not capable of providing global optimal performance for varying operation points, which stimulates lots of research efforts on the tuning of the VC with PI loops.

To improve the performance of the VC-MPPT, a feedback linearizing control (FLC) based MPPT (FLC-MPPT) is designed for the PMSG-WT to extract the maximum wind power [27]. The FLC strategy has been widely applied in power electronics [28, 29], permanent magnet synchronous motor [30], and low voltage ride-through of the PMSG-based WECS [31]. The FLC provides nonlinear systems with better dynamic performances than the controllers designed based on an approximated linear model and linear technique. In [27], the PMSG-WT system is transformed into an equivalent linear system via nonlinear feedback control and state transformation. Then, the closed-loop mechanical rotation speed controller and current controllers are designed via linear control method. The FLC-MPPT can fully decouple the original PMSG-WT system and provide a global optimal controller crossing a wide region and varying operation points. The maximum wind power can be extracted with satisfactory dynamic performances when wind speed varies. However, the design of the FLC-MPPT requires full state feedback and accurate PMSG-WT system model to calculate full system nonlinearities, and this always results in a complex control law and has weak robustness against parameter uncertainties and external disturbances [32].

In the real system operation, some parameters, such as stator resistance, inductance, field flux and other parameters of electrical machine, are affected by operating conditions and manufacturing tolerance, which would deteriorate performance of the FLC [33, 34, 35]. To remedy these shortcomings of the FLC, a high gain perturbation observer based nonlinear adaptive control (HGPONAC) was proposed in the authors' previous work [36], which can improve the robustness of the FLC and remove the dependance of the detailed model of the FLC. Recently, the authors have applied this idea to successfully enhance the fault ride-through capability of the PMSG-WT [37]. It can be expected to improve the MPPT performance of the PMSG-WT operating under time-varying wind speed, parameter uncertainties, and external disturbance conditions by replacing the FLC-MPPT of [27] with the HGPONAC based MPPT (HGPONAC-MPPT).

In this paper, an HGPONAC is developed for the MPPT of the PMSG-WT, aiming to not only improve energy conversion efficiency under time-varying wind power inputs and inaccurate parameters of the WECS, but also provide high robustness against system parameter uncertainties and external disturbances. By defining a lumped perturbation term to present coupling nonlinear dynamics, parameter uncertainties, and other unknown disturbances, a perturbation observer is designed to estimate the lumped perturbation, which then is used to compensate the real perturbation and realize an adaptive linearizing of the original nonlinear system. The HGPONAC-MPPT can fully take into account of all PMSG-WT system nonlinearities and unknown dynamics, and external disturbances caused by tower shadow and time-varying wind speed, without requiring the accurate system model and full state measurements, compared with the FLC-MPPT. The effectiveness of the proposed control scheme is verified through both simulation studies and experimental tests.

The main contributions of this paper are summarized as follows:

- A robust maximum power point tracking (MPPT) control scheme is proposed for a grid-connected PMSG-WT using perturbation observation based nonlinear adaptive control to increases energy conversion efficiency under time-varying wind.
- The high-gain observer is incorporated into original FLC to design the proposed MPPT control scheme, which can fully take into account of all PMSG-WT system nonlinearities and unknown dynamics, and external disturbances, without requiring the accurate system model. Therefore, the proposed approach is robust to generator parameter uncertainties, tower shadow and pitch angle variation.
- Since the high-gain observer can estimate all the system full states accurately, only the input signals are required and full state measurements are not required for the proposed MPPT control scheme. Hence, the proposed control scheme is an output feedback controller, which is easily implemented for a practical system.

- The effectiveness of the proposed control scheme has been verified through both simulation studies and experimental tests.

The remainder of this paper is organized as follows. In Section 2, the model of PMSG-WT and problem formulation are briefly recalled. The design of the HGPONAC-MPPT control scheme, together with an FLC-MPPT, and the stability analysis of the whole closed-loop system are presented in Section 3. In Section 4, simulation studies are conducted to verify the performances of the proposed HGPONAC-MPPT, compared with the VC-MPPT and the FLC-MPPT. Experimental validations are carried out in Section 5. Finally, conclusions are drawn in Section 6.

2. Dynamic Model and Problem Formulation

The configuration of a gearless WECS equipped with a PMSG-WT is shown in Fig. 1, in which wind energy extracted by the wind turbine is transmitted to the PMSG, and the electrical power from the PMSG is then supplied to the power grid through a machine-side converter and a grid-side inverter. The DC voltage link between the converter and the inverter decouples the dynamic and control of the PMSG-WT and the power grid [28]. Two converters are controlled for regulating the output power of the PMSG and delivering active power to the grid, respectively. The MPPT problem concerned in this paper is achieved by controlling mechanical rotation speed via the machine-side converter. Therefore, the dynamic models of the wind turbine and the PMSG controlled by the machine-side converter are given in this section.

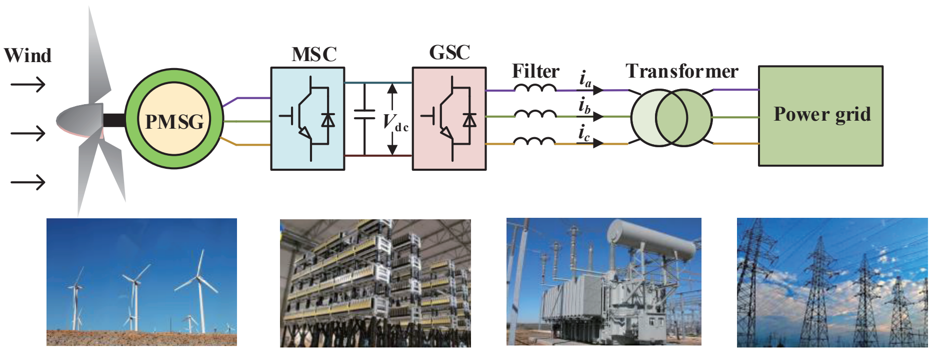

Figure 1: Configuration of PMSG based wind turbine

2.1. Model of the PMSG-WT

2.1.1. Wind turbine

The kinetic power extracted by the wind turbine is given as [38]:

$$P_{\mathrm{w}} = \frac{1}{2}\rho\pi R^2 V^3 C_p(\beta, \lambda) \tag{1}$$

where, ρ is the air density, R is the blade radius, V is the wind speed, C_p is the power coefficient, β is the pitch angle, and λ is the tip speed ratio (TSR) given by

$$\lambda = \frac{R\omega_{\mathrm{m}}}{V} \tag{2}$$

with ω_{m} being the mechanical rotation speed.

The C_p is a function of β and λ, and the following one recalled from [38] is used in this paper:

$$C_p(\beta, \lambda) = 0.22\left(\frac{116}{\lambda_t} - 0.4\beta - 5\right)e^{\frac{-12.5}{\lambda_t}} \tag{3}$$

where

$$\frac{1}{\lambda_t} = \frac{1}{\lambda + 0.08\beta} - \frac{0.035}{\beta^3 + 1} \tag{4}$$

2.1.2. PMSG

The voltage and torque equations of the PMSG in the $d-q$ reference frames are given by [39]

$$V_{\mathrm{d}} = R_{\mathrm{s}} i_{\mathrm{d}} + L_{\mathrm{d}}\frac{\mathrm{d}i_{\mathrm{d}}}{\mathrm{d}t} - \omega_{\mathrm{e}} L_{\mathrm{q}} i_{\mathrm{q}} \tag{5}$$

$$V_{\mathrm{q}} = R_{\mathrm{s}} i_{\mathrm{q}} + L_{\mathrm{q}}\frac{\mathrm{d}i_{\mathrm{q}}}{\mathrm{d}t} + \omega_{\mathrm{e}} L_{\mathrm{d}} i_{\mathrm{d}} + \omega_{\mathrm{e}} K_e \tag{6}$$

$$T_{\mathrm{e}} = p[(L_{\mathrm{d}} - L_{\mathrm{q}}) i_{\mathrm{d}} i_{\mathrm{q}} + i_{\mathrm{q}} K_e] \tag{7}$$

where, V_{d} and V_{q} are the stator voltages in the d-q axis, i_{d} and i_{q} are the stator currents in the d-q axis, R_{s} is the stator resistance, L_{d} and L_{q} are the inductances in the d-q axis, $\omega_{\mathrm{e}}(= p\omega_{\mathrm{m}})$ is the electrical generator rotation speed with p being the number of pole pairs, K_e is the field flux, and T_{e} is the electromagnetic torque. The motion equation of the PMSG is given as

$$J\frac{\mathrm{d}\omega_{\mathrm{m}}}{\mathrm{d}t} = T_{\mathrm{e}} - T_{\mathrm{m}} \tag{8}$$

where, J is the total inertia of the drive train equaling to the summation of wind turbine inertia and generator inertia, and T_{m} is the wind turbine mechanical torque and calculated by

$$T_{\mathrm{m}} = \frac{\rho\pi R^2 V^3 C_p}{2\omega_{\mathrm{m}}} \tag{9}$$

2.2. *MPPT technique based on tip speed ratio (TSR) control*

The paper aims to increase the efficiency of the WECS during the wind turbine working in region 2. Region 2 is the moderate-speed region that is bounded by the cut-in speed at which the wind turbine starts working, and the rated speed at which the wind turbine produces its rated power. In this region, the wind turbine is controlled to extract the maximum power from wind power [21, 40]. To extract the maximum wind power, the power coefficient $C_p(\beta, \lambda)$ should maintain its maximum value $C_{p\max}$ at any wind speed within the operating range. $C_{p\max}$ is achieved by maintaining λ at its optimal value λ_{opt}. From (3) and (4), $C_{p\max}$ is achieved by maintaining TSR λ at its optimal value λ_{opt}, i.e.,

$$C_{p\max} = C_p(\lambda_{\text{opt}}) \tag{10}$$

The λ_{opt} for a given wind turbine is constant regardless of wind speed under a constant pitch angle. TSR control directly regulates the mechanical rotation speed ω_{m} to keep λ at its optimal value λ_{opt} by measuring wind speed and mechanical rotation speed [21, 40, 41]. It requires the mechanical rotation speed ω_{m} to track its optimal reference ω_{mr} from (2):

$$\omega_{\text{mr}} = \frac{\lambda_{\text{opt}}}{R} V \tag{11}$$

The WECS can extract maximum wind energy if mechanical rotation speed ω_{m} can track its optimal reference ω_{mr}. Therefore, this control method seeks to force the WECS to remain at this point by comparing ω_{mr} with the actual value ω_{m} and feeding this difference to the controller. The block diagram of MPPT technique based on TSR control is shown in Fig. 2.

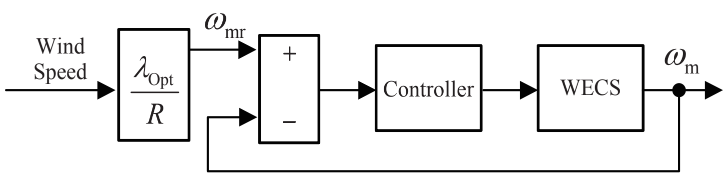

Figure 2: The block diagram of the MPPT technique based on TSR control

In this paper, the function of C_p given in [38] is used, in which the optimal TSR is $\lambda_{\text{opt}} = 7.3089$ and $C_{p\max} = 0.402$. Note that the accurate power coefficient is very important to design control scheme for wind energy conversion system, especially maximum power controller. For a practical wind turbine, the estimated methods proposed in [42, 43, 44] can be used for obtaining the accurate power coefficient.

Several factors, such as time-varying wind speed, parameter uncertainties, and external disturbances, will make the PMSG-WT out of its maximal efficiency condition. Therefore, the purpose of this paper is to develop an adaptive MPPT control scheme based on TSR control, which controls the real time mechanical rotation speed to match its optimal reference ω_{mr} as much as possible, so as to extract maximum wind power in consideration of those uncertainties and disturbances.

3. High Gain Perturbation Observation Based MPPT Control Scheme

This section extends a high gain perturbation observer based nonlinear adaptive control (HGPONAC) to the MPPT problem of the PMSG-WT. The design procedure of the HGPONAC is briefly recalled from our previous work [36]. Then, the detailed MPPT control scheme based on the HGPONAC is presented. Finally, the stability of PMSG-WT with the proposed control scheme is proved.

3.1. High gain perturbation observer based nonlinear adaptive control

The main idea of this control strategy is that a perturbation term is firstly defined to include subsystem nonlinearities, interactions between subsystems, and uncertainties appearing in the input/output linearized system. Its estimated value obtained via an observer is then used to compensate the real perturbation and implement an adaptive linearizing and decoupling control of the original nonlinear system. One can refer to [36] for the detailed theoretical analysis. Here the key design steps for control design are summarized as follows:

Step 1: Model construction. Construct the following standard multi-input multi-output (MIMO) nonlinear system based on the dynamic characteristic of the system:

$$\begin{cases} \dot{x} = f(x) + g(x)u \\ y = h(x) \end{cases} \tag{12}$$

where $x \in r^n$ is the state vector, $u \in r^m$ is the control input vector, $y \in r^m$ is the output vector, and $f(x)$, $g(x)$ and $h(x)$ are some smooth vector functions.

Step 2: Input-output linearization. Differentiating each output y_i of the system until the input u_j appears yields the following input-output relationship:

$$\begin{bmatrix} y_1^{(r_1)} \\ \vdots \\ y_m^{(r_m)} \end{bmatrix} = \begin{bmatrix} L_f^{r_1} h_1 \\ \vdots \\ L_f^{r_m} h_m \end{bmatrix} + B(x) \begin{bmatrix} u_1 \\ \vdots \\ u_m \end{bmatrix} \tag{13}$$

with

$$B(x) = \begin{bmatrix} L_{g_1}L_f^{r_1-1}h_1 & \cdots & L_{g_m}L_f^{r_1-1}h_1 \\ \vdots & \vdots & \vdots \\ L_{g_1}L_f^{r_m-1}h_m & \cdots & L_{g_m}L_f^{r_m-1}h_m \end{bmatrix} \tag{14}$$

where, $y_i^{(r_i)}$ is the r_ith-order derivative of y_i, r_i is the smallest integer so that at least one of the inputs explicitly appears in $y_i^{(r_i)}$, i.e., $L_{g_j}L_f^{r_i-1}h_i(x) \neq 0$ for at least one j, and $B(x)$ is an $m \times m$ control gain matrix.

Step 3: Perturbation definition and system reconfiguration. Assume all nonlinearities of system (13) are unknown, and define perturbation terms as

$$\begin{bmatrix} \Psi_1(x) \\ \vdots \\ \Psi_m(x) \end{bmatrix} = \begin{bmatrix} L_f^{r_1}h_1 \\ \vdots \\ L_f^{r_m}h_m \end{bmatrix} + (B(x) - B_0) \begin{bmatrix} u_1 \\ \vdots \\ u_m \end{bmatrix} \tag{15}$$

where $\Psi_i(x)$ is the perturbation term, and $B_0 = B(x)|_{x=x(0)}$ is the nominal control gain. Then system (13) is rewritten as

$$\begin{bmatrix} y_1^{(r_1)} \\ \vdots \\ y_m^{(r_m)} \end{bmatrix} = \begin{bmatrix} \Psi_1(x) \\ \vdots \\ \Psi_m(x) \end{bmatrix} + B_0 \begin{bmatrix} u_1 \\ \vdots \\ u_m \end{bmatrix} \tag{16}$$

For the ith subsystem, by defining state variables as $z_{i1} = y_i, \cdots, z_{ir_i} = y_i^{(r_i-1)}$ and a virtual state to represent the perturbation $z_{i(r_i+1)} = \Psi_i(x)$, the ith subsystem of (12) can be represented as

$$\begin{cases} \dot{z}_{i1} &= z_{i2} \\ &\vdots \\ \dot{z}_{ir_i} &= z_{i(r_i+1)} + B_{0_i}u \\ \dot{z}_{i(r_i+1)} &= \dot{\Psi}_i(x) \end{cases} \tag{17}$$

where, B_{0_i} is the ith row of the B_0, and $B_{0_{ij}}$ is the ith row jth column element of the B_0.

For system(17), several types of perturbation observers, such as high gain observer, sliding mode observer and linear Luenberger observer, have been proposed [36, 46].

Step 4: High gain perturbation observer (HGPO) design. High gain observer is applied in this paper. For subsystem (17), the output $y_i = z_{i1}$ is measurable, then the following $(r_i + 1)$th-order states and perturbation observer

(SPO) can be designed to estimate the system states and perturbation:

$$\begin{cases} \dot{\hat{z}}_{i1} &= \hat{z}_{i2} + l_{i1}(z_{i1} - \hat{z}_{i1}) \\ & \cdots \\ \dot{\hat{z}}_{ir_i} &= \hat{z}_{i(r_i+1)} + l_{ir_i}(z_{i1} - \hat{z}_{i1}) + B_{0_i} u \\ \dot{\hat{z}}_{i(r_i+1)} &= l_{i(r_i+1)}(z_{i1} - \hat{z}_{i1}), \end{cases} \tag{18}$$

where, $\hat{z}_{ij}$ is the estimations of z_{ij}, and l_{ij} are gains of the high gain observer and designed by

$$l_{ij} = \frac{\alpha_{ij}}{\epsilon_i^j} \tag{19}$$

and ϵ_i is a scalar chosen to be within (0,1) for representing times of the time-dynamics between the observer and the real system, and parameters α_{ij}, $j = 1, \cdots, r_i + 1$, are chosen so that the roots of

$$s^{r_i+1} + \alpha_{i1} s^{r_i} + \cdots + \alpha_{ir_i} s + \alpha_{i(r_i+1)} = 0 \tag{20}$$

are in the open left-half complex plane.

Step 5: Perturbation compensation and linear system control. The actual perturbation $\Psi_i(x)$ of system (16) is compensated by using the estimate of perturbation $\hat{\Psi}_i(x) = \hat{z}_{i(r_i+1)}$ and the following HGPONAC:

$$u_{nac} = B_0^{-1} \left\{ \begin{bmatrix} -\hat{\Psi}_1(x) \\ \vdots \\ -\hat{\Psi}_m(x) \end{bmatrix} + \begin{bmatrix} v_1 \\ \vdots \\ v_m \end{bmatrix} \right\} \tag{21}$$

where, $v_i = -K_i \hat{z}_i$ is an output feedback when SPO is designed. $K_i = [k_{i1}, \cdots, k_{i(r_i-1)}]^T$ is linear control gains which are determined via linear system method.

In addition, from input/output linearlization system (13), the standard feedback linearizing control (FLC) to be compared in this paper is obtained as

$$u_{flc} = B(x)^{-1} \left\{ \begin{bmatrix} -L_f^{r_1} h_1 \\ \vdots \\ -L_f^{r_m} h_m \end{bmatrix} + \begin{bmatrix} v_1 \\ \vdots \\ v_m \end{bmatrix} \right\} \tag{22}$$

where, v_i is designed the same to the one in (21).

The control law u_{flc} is very sensitive to the system parameters and requires system measurements, thus both the parameter uncertainties and disturbance lead to incomplete compensation of perturbation and further degrade the control performance. On the contrary, due to the usage of the perturbation observer, which compensates the actual perturbation, the proposed HGPONAC, u_{nac}, only requires a few measured outputs and the nominal values of the parameters to provide well robustness.

3.2. HGPONAC based MPPT scheme

An adaptive MPPT scheme is designed for the PMSG-WT by following the procedure given in previous.

By choosing measurable signal i_{d} and ω_{m} as outputs, and V_{d} and V_{q} as control inputs, the model given by (5)-(8) can be rewritten as the following state-space system in the form of (12):

$$\begin{cases} \begin{bmatrix} \dot{i}_{\mathrm{d}} \\ \dot{i}_{\mathrm{q}} \\ \dot{\omega}_{\mathrm{m}} \end{bmatrix} = \begin{bmatrix} -\frac{R_{\mathrm{s}}}{L_{\mathrm{d}}} i_{\mathrm{d}} + \frac{\omega_{\mathrm{e}} L_{\mathrm{q}}}{L_{\mathrm{d}}} i_{\mathrm{q}} \\ -\frac{R_{\mathrm{s}}}{L_{\mathrm{q}}} i_{\mathrm{q}} - \frac{1}{L_{\mathrm{q}}} \omega_{\mathrm{e}} (L_{\mathrm{d}} i_{\mathrm{d}} + K_e) \\ \frac{1}{J}\{p[(L_{\mathrm{d}} - L_{\mathrm{q}}) i_{\mathrm{d}} i_{\mathrm{q}} + i_{\mathrm{q}} K_e] - T_{\mathrm{m}}\} \end{bmatrix} + \begin{bmatrix} \frac{1}{L_{\mathrm{d}}} & 0 \\ 0 & \frac{1}{L_{\mathrm{q}}} \\ 0 & 0 \end{bmatrix} \begin{bmatrix} V_{\mathrm{d}} \\ V_{\mathrm{q}} \end{bmatrix} \\ \begin{bmatrix} y_1 \\ y_2 \end{bmatrix} = \begin{bmatrix} i_{\mathrm{d}} \\ \omega_{\mathrm{m}} \end{bmatrix}; \begin{bmatrix} u_1 \\ u_2 \end{bmatrix} = \begin{bmatrix} V_{\mathrm{d}} \\ V_{\mathrm{q}} \end{bmatrix} \end{cases} \tag{23}$$

Carrying out the input/output linearization of system above yields

$$\begin{bmatrix} \dot{y}_1 \\ \ddot{y}_2 \end{bmatrix} = \begin{bmatrix} F_1(x) \\ F_2(x) \end{bmatrix} + B(x) \begin{bmatrix} u_1 \\ u_2 \end{bmatrix} \tag{24}$$

where

$$F_1(x) = \frac{1}{L_{\mathrm{d}}}(-i_{\mathrm{d}} R_{\mathrm{s}} + \omega_{\mathrm{e}} L_{\mathrm{q}} i_{\mathrm{q}}) \tag{25}$$

$$\begin{aligned} F_2(x) = &-\frac{p}{J L_{\mathrm{q}}}[K_e + (L_{\mathrm{d}} - L_{\mathrm{q}}) i_{\mathrm{d}}] L_{\mathrm{d}} \omega_{\mathrm{e}} i_{\mathrm{d}} - \frac{p}{J L_{\mathrm{q}}}[K_e + (L_{\mathrm{d}} - L_{\mathrm{q}}) i_{\mathrm{d}}](R_{\mathrm{s}} i_{\mathrm{q}} + \omega_{\mathrm{e}} K_e) \\ &+ \frac{p i_{\mathrm{q}}}{J L_{\mathrm{d}}}(L_{\mathrm{d}} - L_{\mathrm{q}})(-R_{\mathrm{s}} i_{\mathrm{d}} + L_{\mathrm{q}} \omega_{\mathrm{e}} i_{\mathrm{q}}) - \frac{1}{J}\frac{\mathrm{d}T_{\mathrm{m}}}{\mathrm{d}t} \end{aligned} \tag{26}$$

$$B(x) = \begin{bmatrix} B_1(x) \\ B_2(x) \end{bmatrix} = \begin{bmatrix} \frac{1}{L_{\mathrm{d}}} & 0 \\ \frac{p i_{\mathrm{q}}(L_{\mathrm{d}} - L_{\mathrm{q}})}{J L_{\mathrm{d}}} & \frac{p[K_e + (L_{\mathrm{d}} - L_{\mathrm{q}}) i_{\mathrm{d}}]}{J L_{\mathrm{q}}} \end{bmatrix} \tag{27}$$

and the relative degree is $r_i = [1, 2]$; and $B(x)$ is nonsingular for all nominal operation points since $\det[B(x)] = \frac{p[K_e + (L_{\mathrm{d}} - L_{\mathrm{q}}) i_{\mathrm{d}}]}{J L_{\mathrm{d}} L_{\mathrm{q}}} \neq 0$ as $K_e \neq 0$.

Based on (15) and (24)-(27), the perturbation terms, $\Psi_i(x), i = 1, 2$, are defined as

$$P_{\Psi 1}: \begin{cases} \Psi_1(x) = F_1(x) + (B_1(x) - B_{0_1}) \begin{bmatrix} u_1 \\ u_2 \end{bmatrix} \\ B_{0_1} = [\frac{1}{L_{\mathrm{d0}}} \quad 0] \end{cases} \tag{28}$$

$$P_{\Psi 2}:\begin{cases}\Psi_2(x)=F_2(x)+(B_2(x)-B_{0_2})\begin{bmatrix}u_1\\ u_2\end{bmatrix}\\ B_{0_2}=\begin{bmatrix}\frac{pi_{\mathrm{q}}(L_{\mathrm{d0}}-L_{\mathrm{q0}})}{J_0L_{\mathrm{d0}}} & \frac{p[K_{e0}+(L_{\mathrm{d0}}-L_{\mathrm{q0}})i_{\mathrm{d}}]}{J_0L_{\mathrm{q0}}}\end{bmatrix}\end{cases} \tag{29}$$

where L_{d0}, L_{q0}, J_0, K_{e0}, B_{0_1}, and B_{0_2} are respectively the nominal values of L_{d}, L_{q}, J, K_e, $B_1(x)$, and $B_2(x)$.

Based on (16), (28) and (29) can be rewritten as

$$\begin{bmatrix}\dot{y}_1\\ \ddot{y}_2\end{bmatrix}=\begin{bmatrix}\Psi_1(x)\\ \Psi_2(x)\end{bmatrix}+B_0\begin{bmatrix}u_1\\ u_2\end{bmatrix} \tag{30}$$

where

$$B_0=\begin{bmatrix}B_{0_1}\\ B_{0_2}\end{bmatrix} \tag{31}$$

Based on (16) and (17), by defining new state vectors $z_{11}=i_{\mathrm{d}}$, $z_{12}=\Psi_1(x)$; $z_{21}=\omega_{\mathrm{m}}$, $z_{22}=\dot{\omega}_{\mathrm{m}}$, $z_{23}=\Psi_2(x)$, system (24) can be divided into the following two subsystems

$$S_1:\begin{cases}\dot{z}_{11}=\Psi_1(x)+B_{0_1}\begin{bmatrix}V_{\mathrm{d}}\\ V_{\mathrm{q}}\end{bmatrix}\\ \dot{z}_{12}=\dot{\Psi}_1(x)\\ z_{11}=y_1\end{cases} \tag{32}$$

$$S_2:\begin{cases}\dot{z}_{21}=z_{22}\\ \dot{z}_{22}=\Psi_2(x)+B_{0_2}\begin{bmatrix}V_{\mathrm{d}}\\ V_{\mathrm{q}}\end{bmatrix}\\ \dot{z}_{23}=\dot{\Psi}_2(x)\\ z_{21}=y_2\end{cases} \tag{33}$$

Based on (18), the following two observers are designed, respectively, to estimate the perturbation $\hat{z}_{12}=\hat{\Psi}_1(x)$ and estimate the $\hat{z}_{22}$ and perturbation $\hat{z}_{23}=\hat{\Psi}_2(x)$:

$$S_1:\begin{cases}\dot{\hat{z}}_{11}=\hat{z}_{12}+l_{11}(i_{\mathrm{d}}-\hat{z}_{11})+B_{0_1}\begin{bmatrix}V_{\mathrm{d}}\\ V_{\mathrm{q}}\end{bmatrix}\\ \dot{\hat{z}}_{12}=l_{12}(i_{\mathrm{d}}-\hat{z}_{11})\end{cases} \tag{34}$$

$$S_2:\begin{cases}\dot{\hat{z}}_{21}=\hat{z}_{22}+l_{21}(\omega_{\mathrm{m}}-\hat{z}_{21})\\ \dot{\hat{z}}_{22}=\hat{z}_{23}+l_{22}(\omega_{\mathrm{m}}-\hat{z}_{21})+B_{0_2}\begin{bmatrix}V_{\mathrm{d}}\\ V_{\mathrm{q}}\end{bmatrix}\\ \dot{\hat{z}}_{23}=l_{23}(\omega_{\mathrm{m}}-\hat{z}_{21}),\end{cases}\tag{35}$$

where the gains, $l_{ij}=\frac{\alpha_{ij}}{\epsilon_i^j}, i=1,2, j=1,r_i+1$, are designed based on (19). By using the estimated perturbations to compensate the actual perturbations, the HGPONAC-based control laws for subsystems S_1 and S_2 are obtained from (21) as follows:

$$\begin{bmatrix}u_1\\ u_2\end{bmatrix}=\begin{bmatrix}V_{\mathrm{d}}\\ V_{\mathrm{q}}\end{bmatrix}=B_0^{-1}\begin{bmatrix}v_1-\hat{z}_{12}\\ v_2-\hat{z}_{23}\end{bmatrix}\tag{36}$$

In order to achieve MPPT, the real time mechanical rotation speed, $y_2=\omega_{\mathrm{m}}$, should track its optimal reference $y_{2\mathrm{r}}=\omega_{\mathrm{mr}}=\frac{V}{R}\lambda_{\mathrm{opt}}$. In addition, the current $y_1=i_{\mathrm{d}}$ is controlled to track its reference $y_{1\mathrm{r}}=i_{\mathrm{dr}}=0$. Thus, the $v_{1,2}$ is defined as the following form to control the track errors to be zero:

$$\begin{cases}v_1=k_{11}(y_{1\mathrm{r}}-y_1)+\dot{y}_{1\mathrm{r}}\\ v_2=\ddot{y}_{2\mathrm{r}}+k_{21}(y_{2\mathrm{r}}-y_2)+k_{22}(\dot{y}_{2\mathrm{r}}-\hat{z}_{22})\end{cases}\tag{37}$$

By defining track errors $e_1=y_{1\mathrm{r}}-y_1$ and $e_2=y_{2\mathrm{r}}-y_2$, the error dynamics as the following track error system is obtained:

$$\dot{e}_1+k_{11}e_1=0\tag{38}$$

$$\ddot{e}_2+k_{22}\dot{e}_2+k_{21}e_2=0\tag{39}$$

where, the linear control gains, k_{11},k_{21},k_{22}, are tuned via pole-placement technique.

Finally, the HGPONAC-MPPT control law represented by physical variables, such as currents, inductance, total inertia,field flux and mechanical rotation speed, are summarized as follows:

$$\begin{cases}V_{\mathrm{d}}=L_{\mathrm{d0}}[k_{11}(i_{\mathrm{dr}}-i_{\mathrm{d}})+\dot{i}_{\mathrm{dr}}-\hat{z}_{12}]\\ V_{\mathrm{q}}=-\frac{i_{\mathrm{q}}L_{\mathrm{q0}}(L_{\mathrm{d0}}-L_{\mathrm{q0}})}{K_{e0}+(L_{\mathrm{d0}}-L_{\mathrm{q0}})i_{\mathrm{d}}}[k_{11}(i_{\mathrm{dr}}-i_{\mathrm{d}})+\dot{i}_{\mathrm{dr}}-\hat{z}_{12}]\\ \qquad+\frac{J_0L_{\mathrm{q0}}}{p[K_{e0}+(L_{\mathrm{d0}}-L_{\mathrm{q0}})i_{\mathrm{d}}]}[k_{21}(\omega_{\mathrm{mr}}-\omega_{\mathrm{m}})+k_{22}(\dot{\omega}_{\mathrm{mr}}-\hat{z}_{22})+\ddot{\omega}_{\mathrm{mr}}-\hat{z}_{23}]\end{cases}\tag{40}$$

On the other hand, based on (22) and (24), the standard FLC scheme is obtained as

$$\begin{bmatrix}V_{\mathrm{d}}\\ V_{\mathrm{q}}\end{bmatrix}=B(x)^{-1}\begin{bmatrix}v_1-F_1(x)\\ v_2-F_2(x)\end{bmatrix}=\begin{bmatrix}L_{\mathrm{d}} & 0\\ -\frac{i_{\mathrm{q}}L_{\mathrm{q}}(L_{\mathrm{d}}-L_{\mathrm{q}})}{K_e+(L_{\mathrm{d}}-L_{\mathrm{q}})i_{\mathrm{d}}} & \frac{JL_{\mathrm{q}}}{p[K_e+(L_{\mathrm{d}}-L_{\mathrm{q}})i_{\mathrm{d}}]}\end{bmatrix}\begin{bmatrix}v_1-F_1(x)\\ v_2-F_2(x)\end{bmatrix}\tag{41}$$

and its physical variables based form is given as

$$
\begin{cases}
V_{\mathrm{d}} = L_{\mathrm{d}}[k_{11}(i_{\mathrm{dr}} - i_{\mathrm{d}}) + \dot{i}_{\mathrm{dr}} - F_1(x)] \\
V_{\mathrm{q}} = -\frac{i_{\mathrm{q}} L_{\mathrm{q}}(L_{\mathrm{d}} - L_{\mathrm{q}})}{K_e + (L_{\mathrm{d}} - L_{\mathrm{q}}) i_{\mathrm{d}}}[k_{11}(i_{\mathrm{dr}} - i_{\mathrm{d}}) + \dot{i}_{\mathrm{dr}} - F_1(x)] \\
\qquad + \frac{J L_{\mathrm{q}}}{p[K_e + (L_{\mathrm{d}} - L_{\mathrm{q}}) i_{\mathrm{d}}]}[k_{21}(\omega_{\mathrm{mr}} - \omega_{\mathrm{m}}) + k_{22}(\dot{\omega}_{\mathrm{mr}} - \dot{\omega}_{\mathrm{m}}) + \ddot{\omega}_{\mathrm{mr}} - F_2(x)]
\end{cases}
\tag{42}
$$

The FLC-MPPT control law (42) requires real values of system parameters and the measurements of wind speed, currents, ω_{m} and $\frac{\mathrm{d}T_{\mathrm{m}}}{\mathrm{d}t}$. On the contrary, the proposed HGPONAC-MPPT control law (40) only requires the nominal values L_{d0}, L_{q0}, K_{e0} and J_0, and the measurements of wind speed, currents and w_{m}. It clearly shows the advantages of the proposed control law, including better robustness and easy realization.

To clearly illustrate the principle of the proposed HGPONAC-MPPT, the block diagram of the proposed HGPONAC-MPPT is depicted in Fig. 3.

3.3. Stability analysis of closed-loop system

This section analyzes the stability of the closed-loop system equipped with the HGPONAC-MPPT designed in the previous section.

At first, both the estimation error system and the tracking error system are obtained. On one hand, by defining estimation errors $\varepsilon_{11} = z_{11} - \hat{z}_{11}$, $\varepsilon_{12} = z_{12} - \hat{z}_{12}$, $\varepsilon_{21} = z_{21} - \hat{z}_{21}$, $\varepsilon_{22} = z_{22} - \hat{z}_{22}$, $\varepsilon_{23} = z_{23} - \hat{z}_{23}$, subtracting (34) from (32) and subtracting (35) from (33) , the following estimation error system yields:

$$
\dot{\varepsilon}_i = A_i \varepsilon_i + \eta_i \tag{43}
$$

where

$$
\varepsilon_i = \begin{bmatrix} \varepsilon_{11} \\ \varepsilon_{12} \\ \varepsilon_{21} \\ \varepsilon_{22} \\ \varepsilon_{23} \end{bmatrix}, \quad
A_i = \begin{bmatrix} -l_{11} & 1 & 0 & 0 & 0 \\ -l_{12} & 0 & 0 & 0 & 1 \\ 0 & 0 & -l_{21} & 1 & 0 \\ 0 & 0 & -l_{22} & 0 & 1 \\ 0 & 0 & -l_{23} & 0 & 0 \end{bmatrix}, \quad
\eta_i = \begin{bmatrix} 0 \\ \dot{\Psi}_1 \\ 0 \\ 0 \\ \dot{\Psi}_2 \end{bmatrix}
\tag{44}
$$

On the other hand, define the tracking errors as $e_{11} = y_{1\mathrm{r}} - z_{11}$, $e_{21} = y_{2\mathrm{r}} - z_{21}$ and $e_{22} = \dot{y}_{2\mathrm{r}} - z_{22}$. It follows from (33) that $\dot{e}_{21} = e_{22}$.

And, it follows from (30), (36) and (37) that

$$
\begin{bmatrix} \dot{e}_{11} \\ \dot{e}_{22} \end{bmatrix} = -\begin{bmatrix} k_{11}(e_{11} + \varepsilon_{11}) + \varepsilon_{12} \\ k_{21}(e_{21} + \varepsilon_{21}) + k_{22}(e_{22} + \varepsilon_{22}) + \varepsilon_{23} \end{bmatrix}
\tag{45}
$$

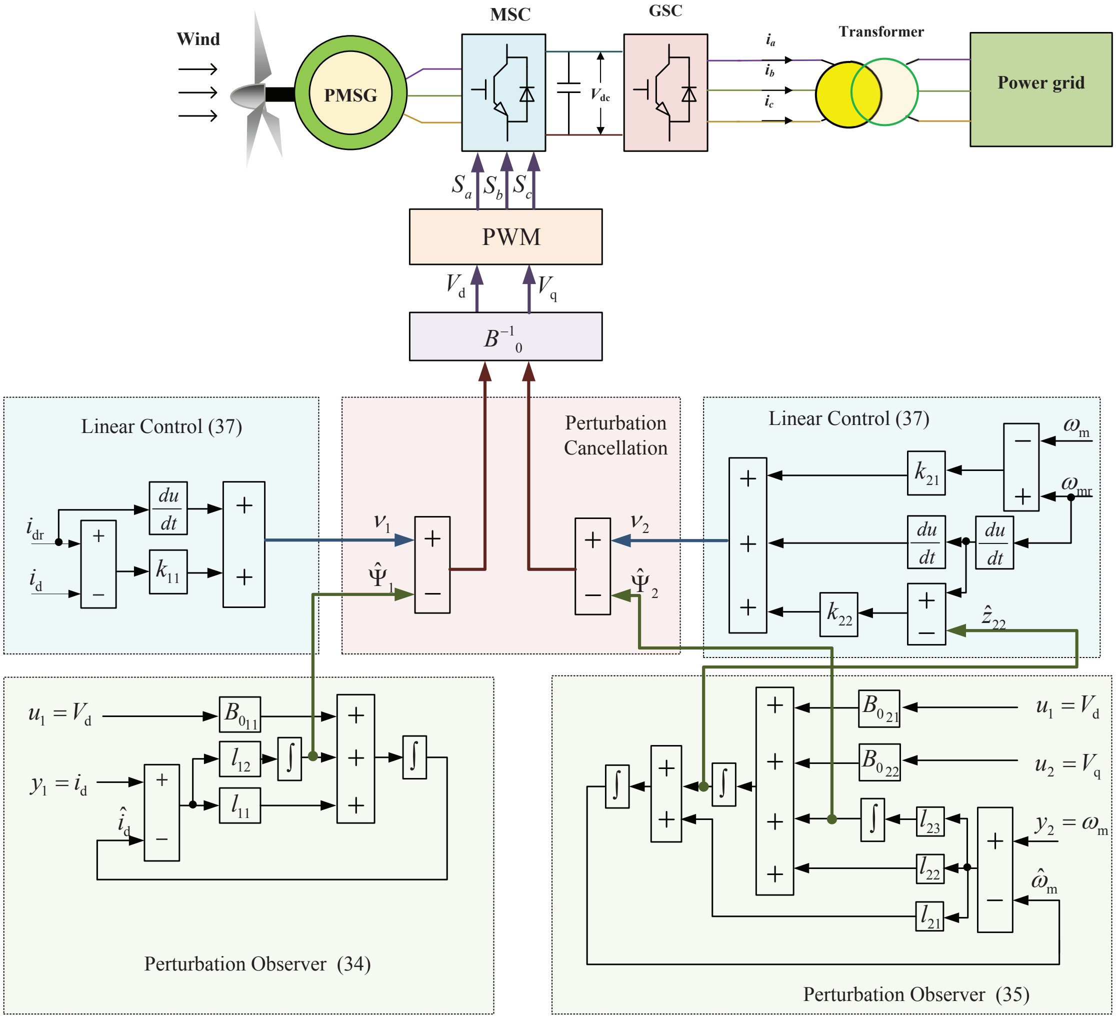

Figure 3: The HGPONAC-MPPT control scheme for the PMSG-WT system

Thus, the tracking error system can be summarized as

$$\dot{e}_i = M_i e_i + \vartheta_i \tag{46}$$

where

$$e_i = \begin{bmatrix} e_{11} \\ e_{21} \\ e_{22} \end{bmatrix}, \quad M_i = \begin{bmatrix} -k_{11} & 0 & 0 \\ 0 & 0 & 1 \\ 0 & -k_{21} & -k_{22} \end{bmatrix}, \quad \vartheta_i = \begin{bmatrix} -\xi_1 \\ 0 \\ -\xi_2 \end{bmatrix} \tag{47}$$

with $\xi_1 = \varepsilon_{12}$ and $\xi_2 = k_{21}\varepsilon_{21} + k_{22}\varepsilon_{22} + \varepsilon_{23}$ being the lumped estimation error.

The stability analysis of the closed-loop control system is transformed into globally uniformly ultimately bounded summarized.

Theorem 1. Consider the PMSG-WT system (24) equipped the proposed HGPONAC (40) with two POs (28) and (29). If the real perturbation $\Psi_i(x,t)$ defined in (28) and (29) satisfies

$$||\Psi_i(x,t)|| \leq \gamma_1 \tag{48}$$

then both the estimation error system (43) and the tracking error system (46) are GUUB, i.e.,

$$||\varepsilon_i(t)|| \leq 2\gamma_1||P_1||, ||e_i(t)|| \leq 4\gamma_1||K_i||||P_1||||P_2||, \forall t \geq T \tag{49}$$

where $P_i, i = 1, 2$ are respectively the feasible solutions of Riccati equations $A_i^{\mathrm{T}}P_1 + P_1A_i = -I$ and $M_i^{\mathrm{T}}P_2 + P_2M_i = -I$; and $||K_i||$ is a constant related to k_{11}, k_{21} and k_{22}.

Proof. For the estimation error system (43), consider the following Lyapunov function:

$$V_{i1}(\varepsilon_i) = \varepsilon_i^{\mathrm{T}}P_1\varepsilon_i \tag{50}$$

The high gains of POs (34) and (35) are determined by requiring (20) holds, which means A_i is Hurwitz. One can find a feasible positive definite solution, P_1, of Riccati equation $A_i^{\mathrm{T}}P_1 + P_1A_i = -I$. Calculating the derivative of $V_{i1}(\varepsilon_i)$ along the solution of system (43) and using (48) to yield

$$\begin{aligned}\dot{V}_{i1}(\varepsilon_i) &= \varepsilon_i^{\mathrm{T}}(A_i^{\mathrm{T}}P_1 + P_1A_i)\varepsilon_i + \eta_i^{\mathrm{T}}P_1\varepsilon_i + \varepsilon_i^{\mathrm{T}}P_1\eta_i \\ &\leq -||\varepsilon_i||^2 + 2||\varepsilon_i|| \cdot ||\eta_i|| \cdot ||P_1|| \\ &\leq -||\varepsilon_i||(||\varepsilon_i|| - 2\gamma_1||P_1||)\end{aligned} \tag{51}$$

Then $\dot{V}_{i1}(\varepsilon_i) \leq 0$ when $||\varepsilon_i|| \geq 2\gamma_1||P_1||$. Thus there exists $T_1 > 0$, which can lead to

$$||\varepsilon_i(t)|| \leq \gamma_2 = 2\gamma_1||P_1||, \forall t \geq T_1 \tag{52}$$

For tracking error system (46), one can find that $||\vartheta_i|| \leq ||K_i||\gamma_2$ with $||K_i||$ based on $||\varepsilon_i(t)|| \leq \gamma_2$. Consider the Lyapunov function $V_{i2}(e_i) = e_i^{\mathrm{T}}P_2e_i$. Similarly, one can prove that, there exists an instant, T_1, the following holds

$$||e_i(t)|| \leq 2||K_i||\gamma_2||P_2|| \leq 4\gamma_1||K_i||||P_1||||P_2||, \forall t \geq \bar{T}_1 \tag{53}$$

Using (52) and (53) and setting $T = \max\{T_1, \bar{T}_1\}$ lead to (49).

Moreover, if W_i is locally Lipschitz in its arguments, it will guarantee the exponential convergence of the observation error [46] and closed-loop tracking error into

$$\lim_{t\to\infty} \varepsilon_i(t) = 0 \text{ and } \lim_{t\to\infty} e_i(t) = 0 \tag{54}$$

After the states ω_{m} and i_{d} and their derivatives are stable that controlled by HGPONAC. The parameter variation is considered in the error system in (43) and (46), and the error system is proved as converged to zero in (54). This guarantees that the estimated perturbations track the extended states defined in (28) and (29), which includes the uncertainties affected by the parameter variations and disturbances, and compensated the control input in (36). Then the linearized subsystems in (32) and (33) are independent of the parameters and disturbances.

Table 1: Parameters of PMSG-WT for simulation study

Parameters	Values	Units
Blade radius R	39	m
Air density ρ	1.205	kg/m^3
Rated wind speed V_r	12	m/s
Rated output power P_g	2	MW
Pitch angle β	2	$^\circ$
Stator resistance R_s	50	$\mu\Omega$
inductance in d-axis L_d	0.0055	H
inductance in q-axis L_q	0.00375	H
Number of pole pairs p	11	
Field flux K_e	136.25	$V \cdot s/rad$
Total inertia J	10,000	$kg \cdot m^2$

4. Simulation Validation

Simulation studies are carried out to verify the performance of the proposed HGPONAC-MPPT scheme in comparing with the VC-MPPT and FLC-MPPT. A 2 MW PMSG-WT discussed in [38] is used and its parameters are listed in Table 1. Moreover, the control parameters designed in this paper and reported in [37, 45] are summarized

Table 2: Parameters of MPPT control schemes for simulation study

Parameters of the HGPONAC-MPPT (40)		
Gains of observer (34)	(20)	$pole = 160, \alpha_{11} = 2 \times 160 = 320$, $\alpha_{12} = 160^2$
	(19)	$\epsilon_1 = 0.02$, $l_{11} = \frac{\alpha_{11}}{\epsilon_1} = 1.6 \times 10^4$, $l_{12} = \frac{\alpha_{12}}{\epsilon_1^2} = 6.4 \times 10^7$
Gains of observer (35)	(20)	$pole = 500, \alpha_{21} = 3 \times 500 = 1.5 \times 10^3$, $\alpha_{22} = 3 \times 500^2 = 7.5 \times 10^5$,
		$\alpha_{23} = 500^3 = 1.25 \times 10^8$
	(19)	$\epsilon_2 = 0.02$, $l_{21} = \frac{\alpha_{21}}{\epsilon_2} = 7.5 \times 10^4$, $l_{22} = \frac{\alpha_{22}}{\epsilon_2^2} = 1.875 \times 10^9$, $l_{23} = \frac{\alpha_{23}}{\epsilon_2^3} = 1.5625 \times 10^{13}$
Gains of linear controller (37)		$k_{11} = 16$, $k_{21} = 2500$, $k_{22} = 100$
Parameters of the FLC-MPPT (42)		
Gains of linear controller (37)		$k_{11} = 16$, $k_{21} = 2500$, $k_{22} = 100$

in Table 2. Four scenarios, including random wind speed, parameter uncertainties, tower shadow, and pitch angle variation are used to illustrate the advantages of the proposed HGPONAC-MPPT.

4.1. Operation under random wind speed condition

4.1.1. Comparison of VC-MPPT, FLC-MPPT, and HGPONAC-MPPT

The PMSG-WT operating under random wind speed condition depicted in Fig. 4 (a) is tested at first. The wind speed is lower than the rated speed of wind turbine, 12m/s, thus the wind turbine is working in region 2 and is controlled to extract the maximum power. The responses of the PMSG-WT are illustrated in Fig. 4(b)-(f).

Fig. 4(b) and (c) shows the performance of real-time mechanical rotation speed $\omega_{\rm m}$ tracking its optimal value, $\omega_{\rm mr}$. It can be seen that the proposed HGPONAC-MPPT provides the best tracking performance in comparing with both the VC-MPPT and the FLC-MPPT. The relative errors between $\omega_{\rm m}$ and its optimal value (calculated by $\frac{\omega_{\rm m}-\omega_{\rm mr}}{\omega_{\rm mr}} \times 100\%$) are respectively within $\pm 1\%$ for the HGPONAC-MPPT, $\pm 3\%$ for the FLC-MPPT, and 10% for the VC-MPPT. The maximum relative error is up to 10% under the VC-MPPT. This is because the VC-MPPT is designed based on one specific operation point of the system and cannot ensure a satisfied dynamic behavior for time-varying wind speed case. Compared with the HGPONAC-MPPT, the decrease of tracking performance provided by the FLC-MPPT is caused by the fact that the FLC-MPPT requires full state measurements, while the $\frac{{\rm d}T_{\rm m}}{{\rm d}t}$ in FLC-MPPT control law is unknown.

Basing on (10) and (11), the power extracting coefficient C_p is dependent on the tracking performance of $\omega_{\rm m}$.

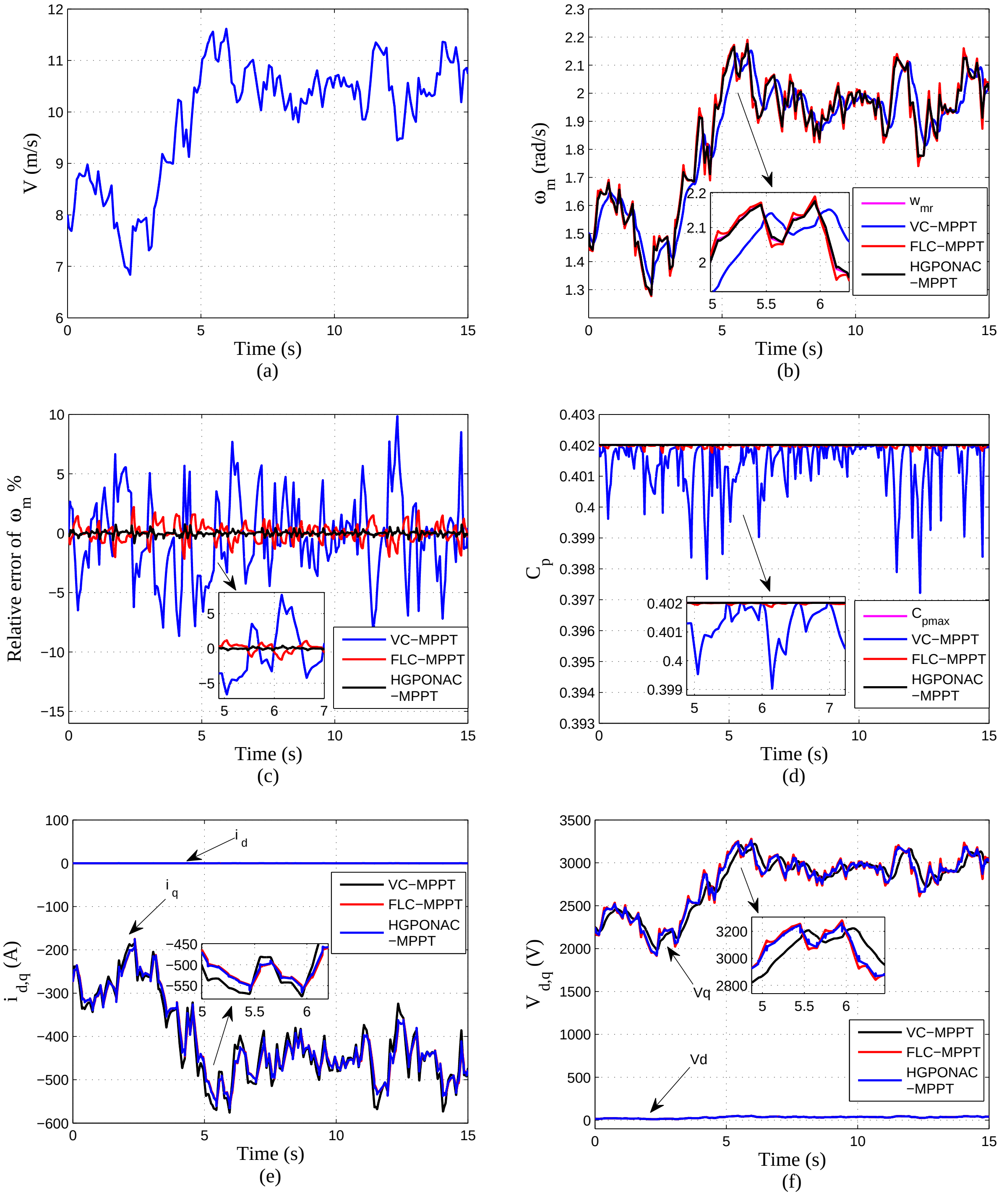

Figure 4: Responses to random wind speed. (a) Wind speed; (b) Mechanical rotation speed; (c) Relative error of mechanical rotation speed; (d) Power coefficient; (e) Stator currents $i_{\mathrm{d,q}}$; and (f) Stator voltages $V_{\mathrm{d,q}}$.

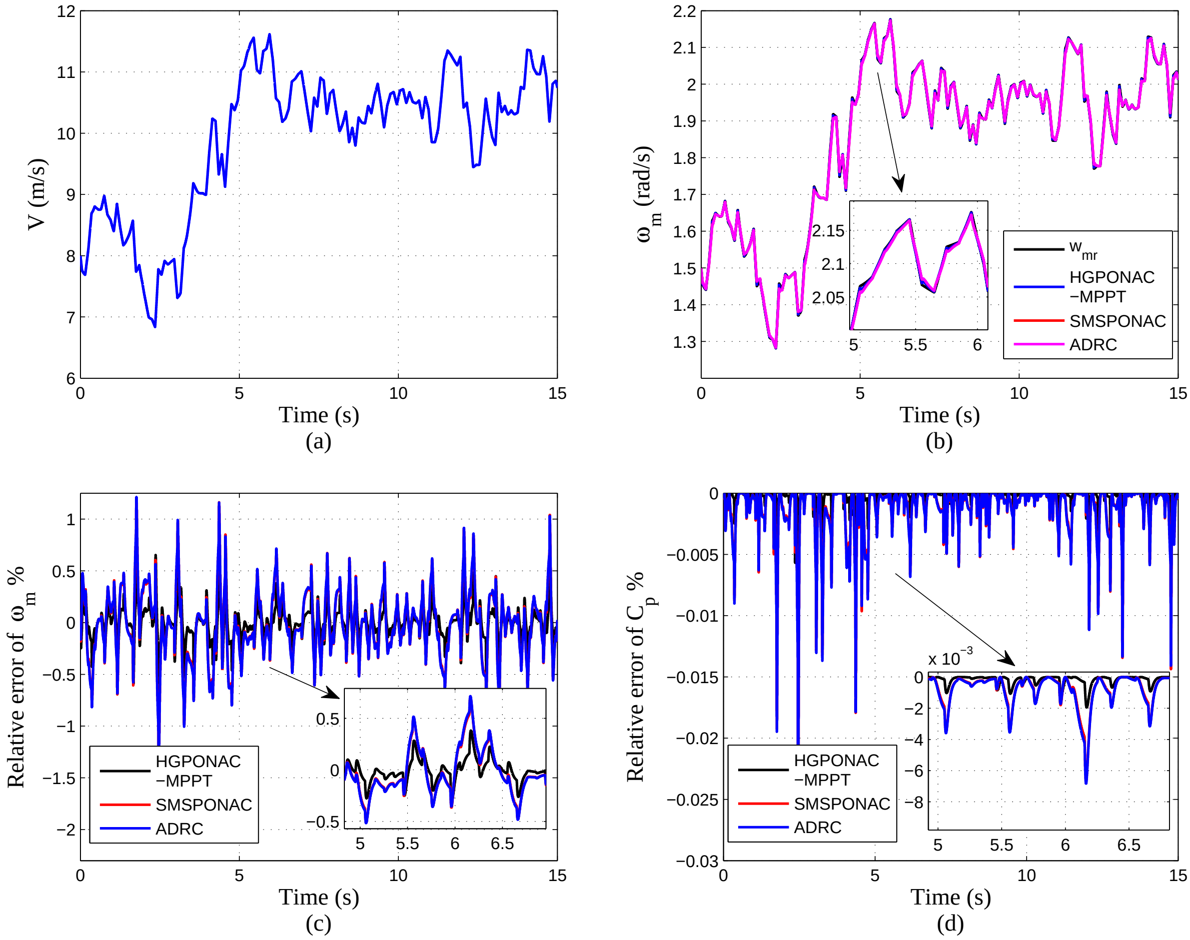

Figure 5: Responses to random wind speed under different observer based control methods. (a) Wind speed; (b) Mechanical rotation speed; (c) Relative error of mechanical rotation speed; and (d) Relative error of power coefficient.

Such relationship is indicated from the results of Fig. 4(d), in which the power coefficient $C_{p\max}$ is always quite close to its maximum value under the HGPONAC-MPPT, and has only a few small deviation for the FLC-MPPT, while it decreases obviously, up to 1%, away from its optimal value for the VC-MPPT. That means for a time-varying wind speed (smaller than rated speed) operation condition, the wind turbine equipped with the proposed HGPONAC-MPPT has potential to extract the most wind power, compared with that with the FLC-MPPT or the VC-MPPT. The stator current and voltage waveforms are given in Fig. 4(e) and (f), respectively.

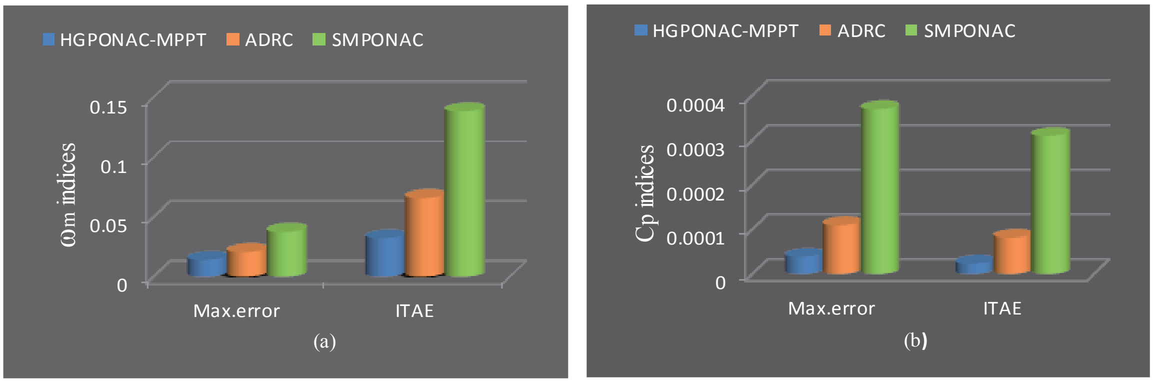

Figure 6: Control performance indices comparison in maximum error and ITAE under random wind speed condition. (a) ω_{m} indices; and (b) C_{p} indices.

4.1.2. Comparison of different observer based control methods

To compare with different observer based control methods, sliding-mode perturbation observer based NAC (SMPONAC) in [46] and nonlinear perturbation observer based active disturbance rejection control (ADRC) [47] are used for comparison in this section. The different perturbation observers are used to estimate the perturbation of system (12) under random wind speed condition shown in Fig. 5(a). The mechanical speed response controlled by different controllers is shown in Fig. 5(b) and (c). Fig. 5(d) shows the power coefficient response. It cane found from Fig. 6 that, the control performance of the HGPONAC-MPPT is better than that of the SMPONAC and ADRC in terms of the maximum regulation error and integral of the time multiplied by the absolute error (ITAE). In addition, the HGPO is simple in structure, gain tuning and stability analysis.

Among the VC-MPPT, FLC-MPPT, and observer-based control methods (such as HGONAC-MPPT), the VC-MPPT is relatively computationally faster, and observer-based control methods has relatively more computation burden duo to observation of states and perturbations, but the acceleration of microprocessor computation speed makes it easier for the controller to realize the proposed control scheme [33].

4.2. Operation under parameter uncertainty condition

4.2.1. Comparison of FLC-MPPT and HGPONAC-MPPT

For a practically equipped PMSG-WT, especially after working for a quite long time, there may possibly exist a gap between its currently actual parameters and the nominal ones given by the manufacturer and used for control design. The control performance of the proposed HGPONAC-MPPT and the standard FLC-MPPT is tested under

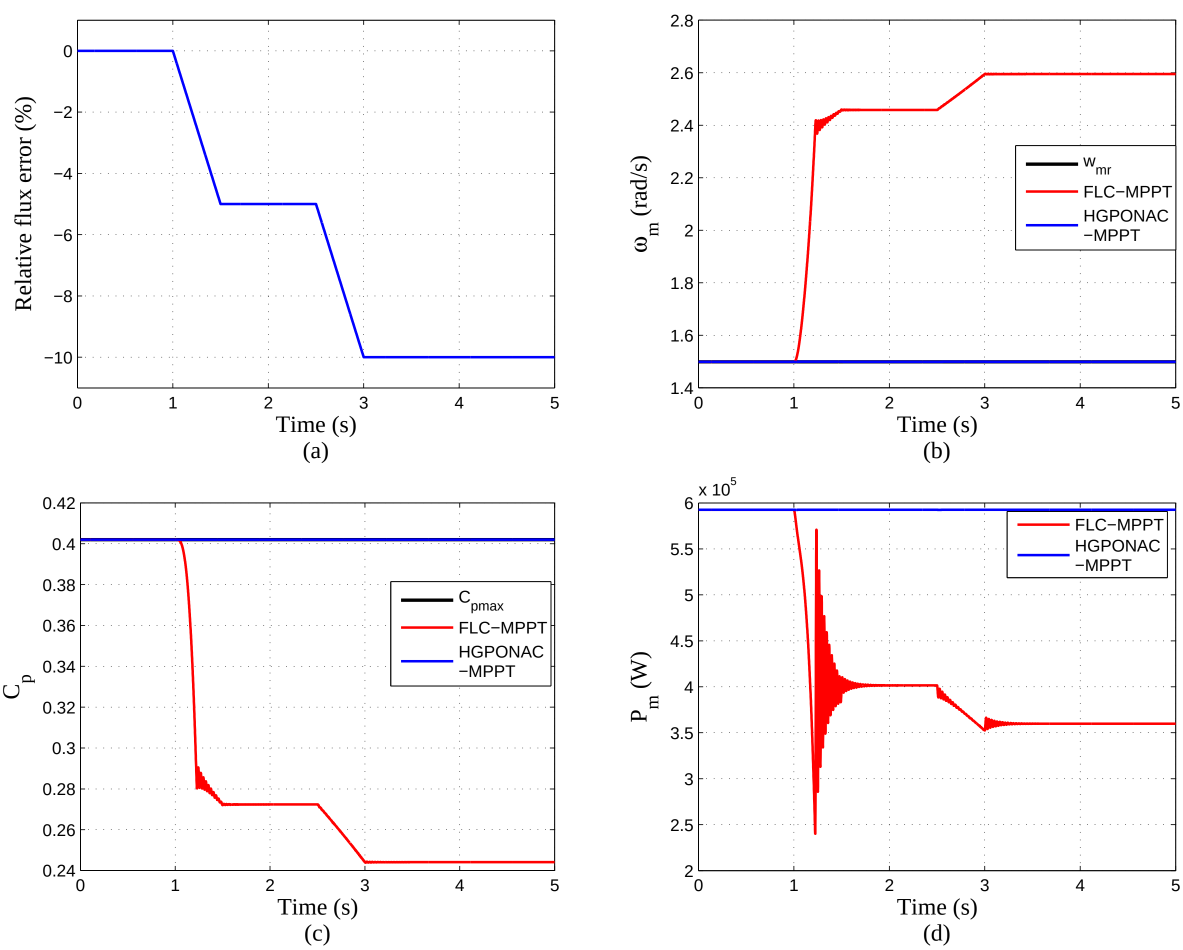

Figure 7: Responses to field flux K_e variation. (a) Deviation of field flux; (b) Mechanical rotation speed; (c) Power coefficient; and (d) Active power.

this parameter mismatch operation condition. Note that wind speed V keeps at 8 m/s during the simulation tests. The mismatch of various parameters are simulated, the results for the mismatch of field flux K_e decreasing from its nominal value to 90% of nominal value, shown in Fig. 7(a), are given. Only the results under the HGPONAC-MPPT and the FLC-MPPT are given since the advantage of the HGPONAC-MPPT in compared with the VC-MPPT is clearly found in the pervious part.

From Fig. 7(b), it can be found that the mechanical rotation speed ω_{m} well tracks its optimal value under the HGPONAC-MPPT, while under the FLC-MPPT, it begins to deviate from its optimal value after the decreasing of the field flux parameter at 1s and the deviation value is approximately up to the 60% of the optimal value. Such large deviation obviously leads to the decreasing of the power coefficient C_p, as clearly shown in Fig. 7(c), in which the

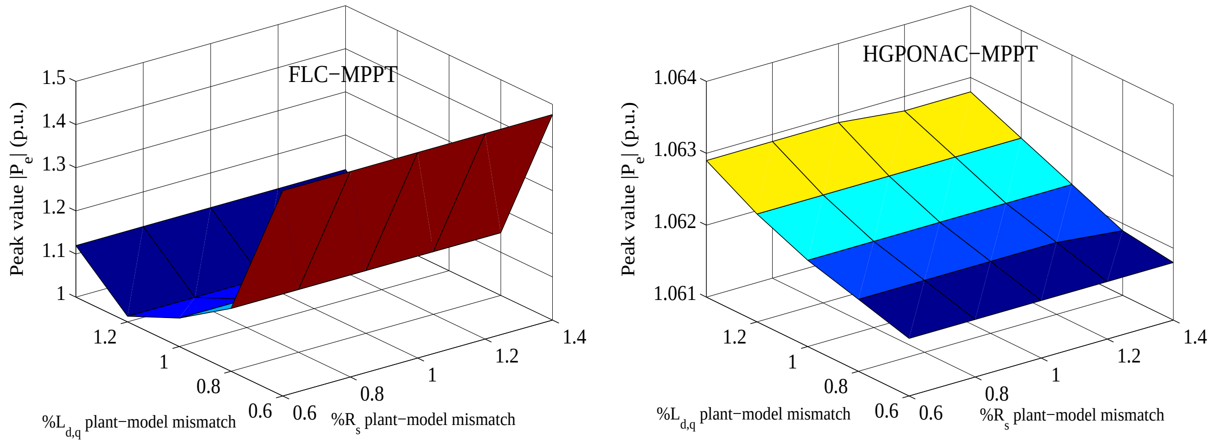

Figure 8: Peak value of active power $|P_{\mathrm{e}}|$ obtained under a 2 m/s wind speed step increase from 10 m/s with 40% variation of the stator resistance R_{s} and inductance $L_{\mathrm{d,q}}$ of different approaches, respectively.

coefficient C_p for the HGPONAC-MPPT is always well maintained at its maximum value while that for the FLC-MPPT is greatly smaller than maximum value during the field flux changing period. Therefore, the power extracted by the PMSG equipped with FLC-MPPT has an approximate 40% decrement of maximum power that extracted by the one equipped with HGPONAC-MPPT, as shown in Fig. 7(d). The decreasing of the performance of the FLC-MPPT following the deviation of field flux K_e is caused by the fact that the control effort produced by the FLC-MPPT scheme (42) is not desired due to the usage of inaccurate field flux. On the contrary, benefit of waiving the requirement of accurately current values of parameters, the proposed HGPONAC-MPPT almost always provides satisfactory performances.

In Fig. 8, a series of plant-model mismatches of stator resistance R_s and inductance $L_{d,q}$ with ±40% variations around their nominal value are undertaken, in which a 2 m/s wind speed step increase from 10 m/s is applied. The peak value of active power $|P_{\mathrm{e}}|$ is recorded for a clear comparison. Fig. 8 shows that the variation of $|P_{\mathrm{e}}|$ obtained by FLC-MPPT and HGPONAC-MPPT is around 46.3% and 0.11%, respectively. This can be explained as follows, the proposed HGPONAC-MPPT estimates all uncertainties and does not need the accurate system model and thus has better robustness than FLC-MPPT which requires an accurate system model.

4.2.2. *Comparison of different observer based control methods*

The HGSPONAC-MPPT, SMPONAC and ADRC are used for comparison of control performance under field flux variation shown in Fig. 9(a). Fig. 9(b)-(d) shows the mechanical rotation speed response and power coefficient response, respectively. Fig. 10 shows performance of different observer based control methods through the maximum regulation error and ITAE. The results show that all different observer based control methods provide high robustness against parameter uncertainty. Moreover, it can also be found that the control performance of the HGPONAC-MPPT is better than that of the SMPONAC and ADRC in terms of both the maximum regulation error and ITAE.

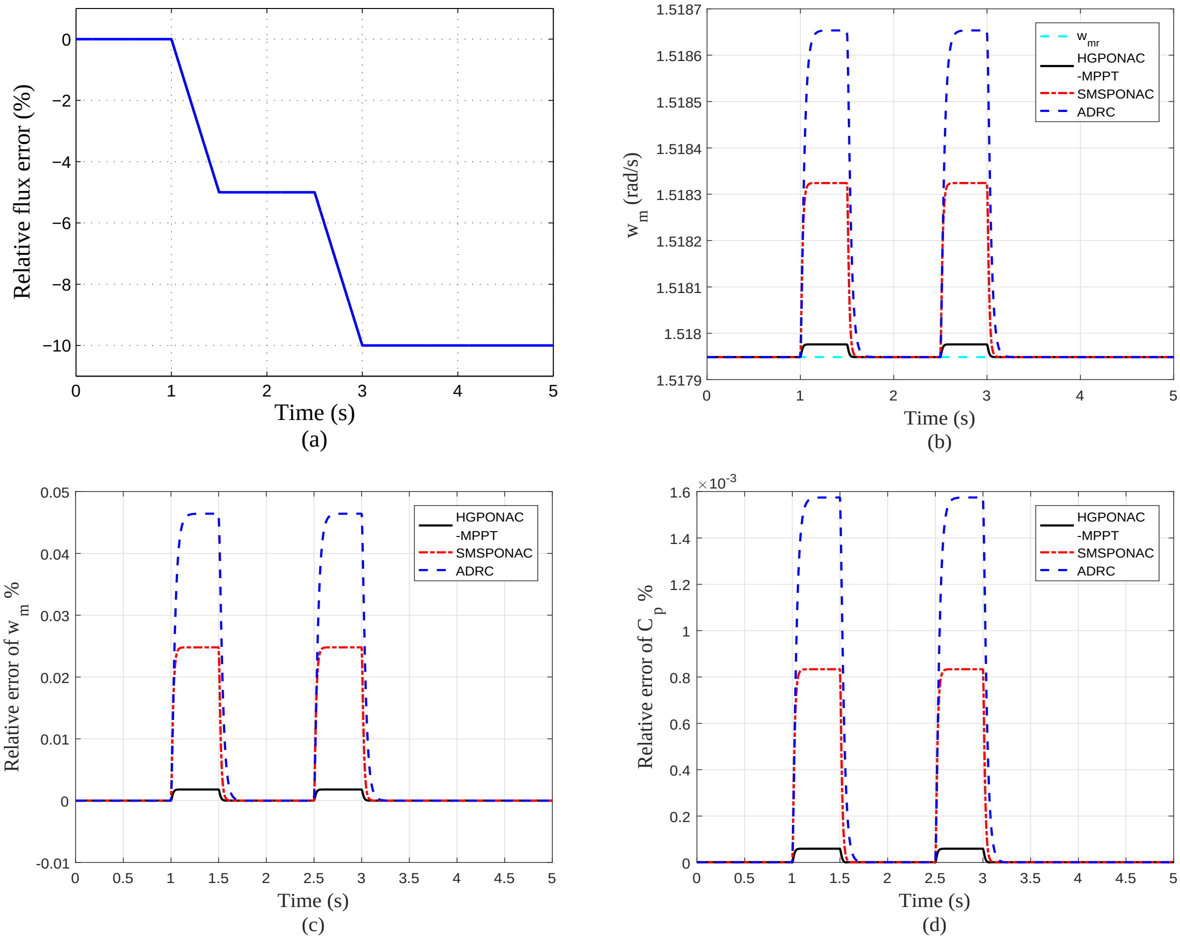

Figure 9: Responses to field flux K_e variation under different observer based control methods. (a) Deviation of field flux; (b) Mechanical rotation speed; (c) Relative error of mechanical rotation speed; and (d) Relative error of power coefficient.

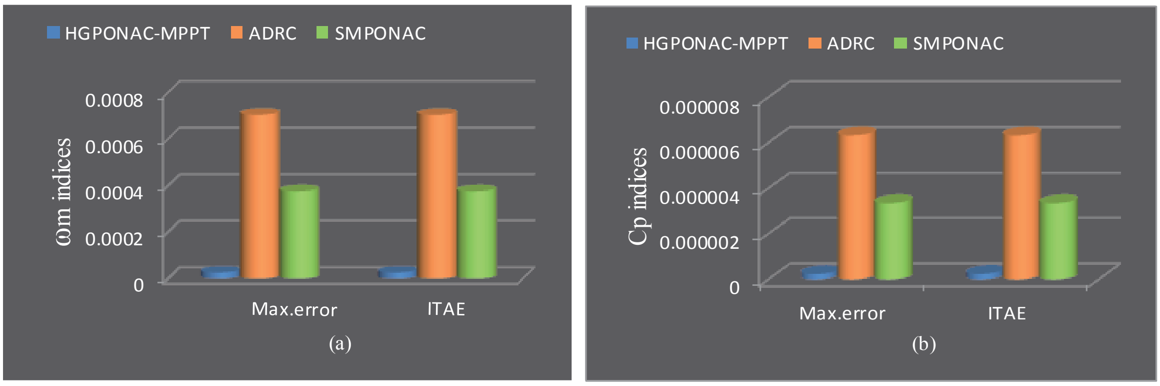

Figure 10: Control performance indices comparison in maximum error and ITAE under field flux variation. (a) ω_{m} indices; and (b) C_{p} indices.

4.3. Operation under tower shadow condition

Tower shadow, describing the redirection of wind due to the presentence of the tower, is an inherent characteristic of wind turbines, and it would produce a periodic pulse reduction in torque when each blade passes by the tower and further leads to periodic fluctuations in electrical power output of a wind turbine generator [48]. Assume the wind turbine with three blades, the simulation tests in consideration of the tower shadow are discussed.

During the simulation study, the optimal reference mechanical rotation speed, ω_{mr}, is calculated by (2) using the measured wind speed from anemometer (Assume the measured wind speed is fixed to 8m/s). As reported in [48], the wind turbine operating under such constant wind speed and considering the effect of tower shadow is equivalent to the wind turbine without considering the effect of tower shadow and operating under an equivalent wind speed, shown in Fig. 11(a), which is reduced by 3% from measurement wind speed as a blade passes in front of the tower, and the duration time of the blade passes the tower is represented by an arc of 40° in one cycle [48]. Based on Eq. (9), the mechanical torque T_{m} will decrease as a blade passes in front of the tower, as shown in Fig. 11(b). The results of Fig. 11(c) and (d) show that the mechanical rotation speed cannot be well tracked under the FLC-MPPT, and the maximum relative error ($\frac{\omega_{\mathrm{m}}-\omega_{\mathrm{mr}}}{\omega_{\mathrm{mr}}} \times 100\%$) is up to 0.5%. This is because that the torque variation $\frac{\mathrm{d}T_{\mathrm{m}}}{\mathrm{d}t}$ caused by the tower shadow is unmeasurable in FLC-MPPT (42). That is, the FLC-MPPT cannot provide the robustness against some external disturbances like tower shadow. On the contrary, the HGPONAC-MPPT scheme can still provide a desirable tracking performance of ω_{m} under the period of torque drop due to no torque measurement required by HGPONAC-MPPT (40).

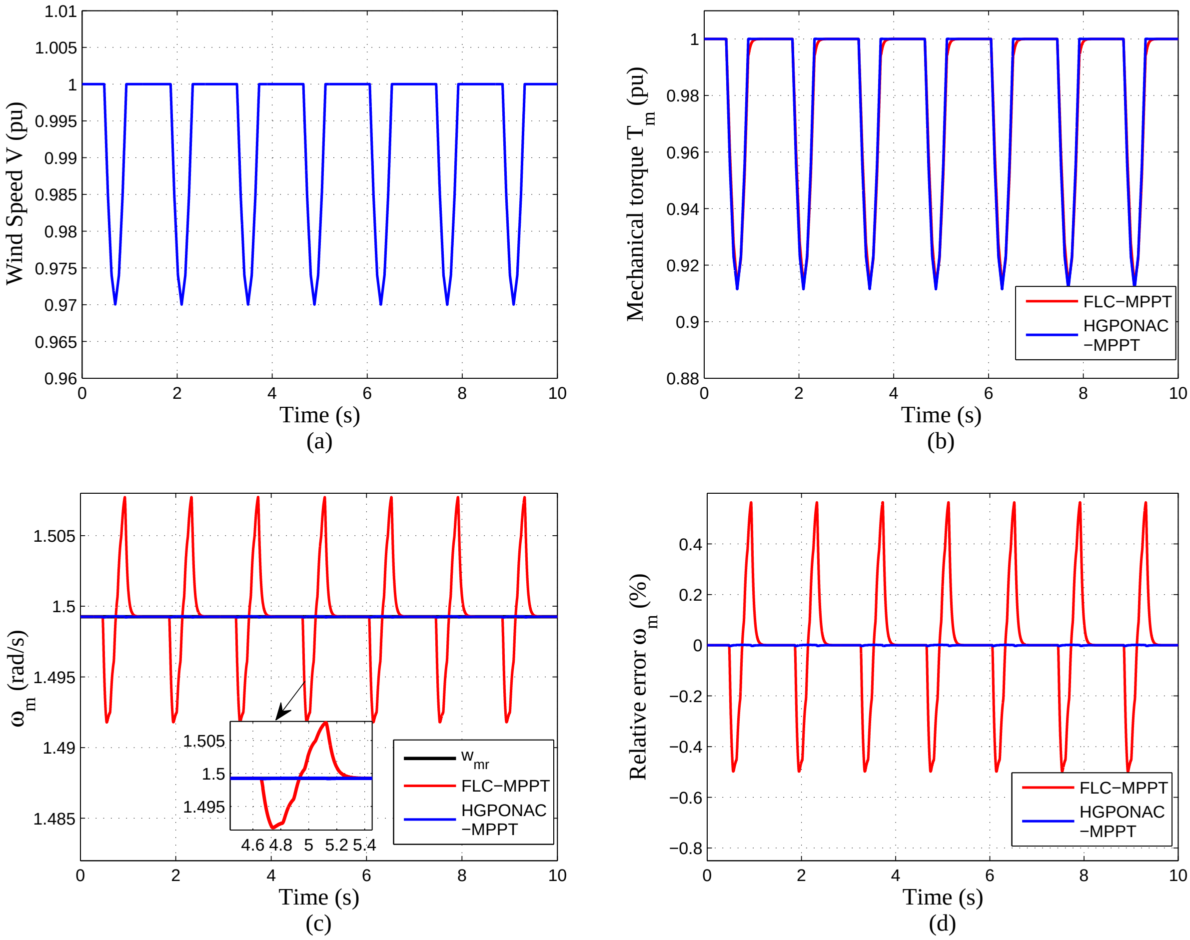

Figure 11: Responses considering tower shadow effect. (a) Equivalent wind speed; (b) Tower effect on the mechanical torque; (c) Mechanical rotation speed; and (d) Relative error of mechanical rotation speed.

4.4. Pitch angle variation

When a pitch angle decreases from 2 degree to 0 degree in 0.3 s under a constant wind speed 12 m/s, the performance of the system with different MPPT control scheme is shown in Fig. 12. It is obvious that the mechanical rotation speed ω_{m} of VC-MPPT achieves the worst performance with longest time to reach steady state, when operation point shifts from the normal operation condition. The FLC-MPPT and HGPONAC-MPPT can reach the new steady state at the much faster rate than the VC-MPPT. Moreover, compared with the FLC-MPPT, the HGONAC-MPPT provides better tracking performance of ω_{m} since the $\frac{\mathrm{d}T_{\mathrm{m}}}{\mathrm{d}t}$ caused by the pitch angle variation is unmeasurable in FLC-MPPT (42).

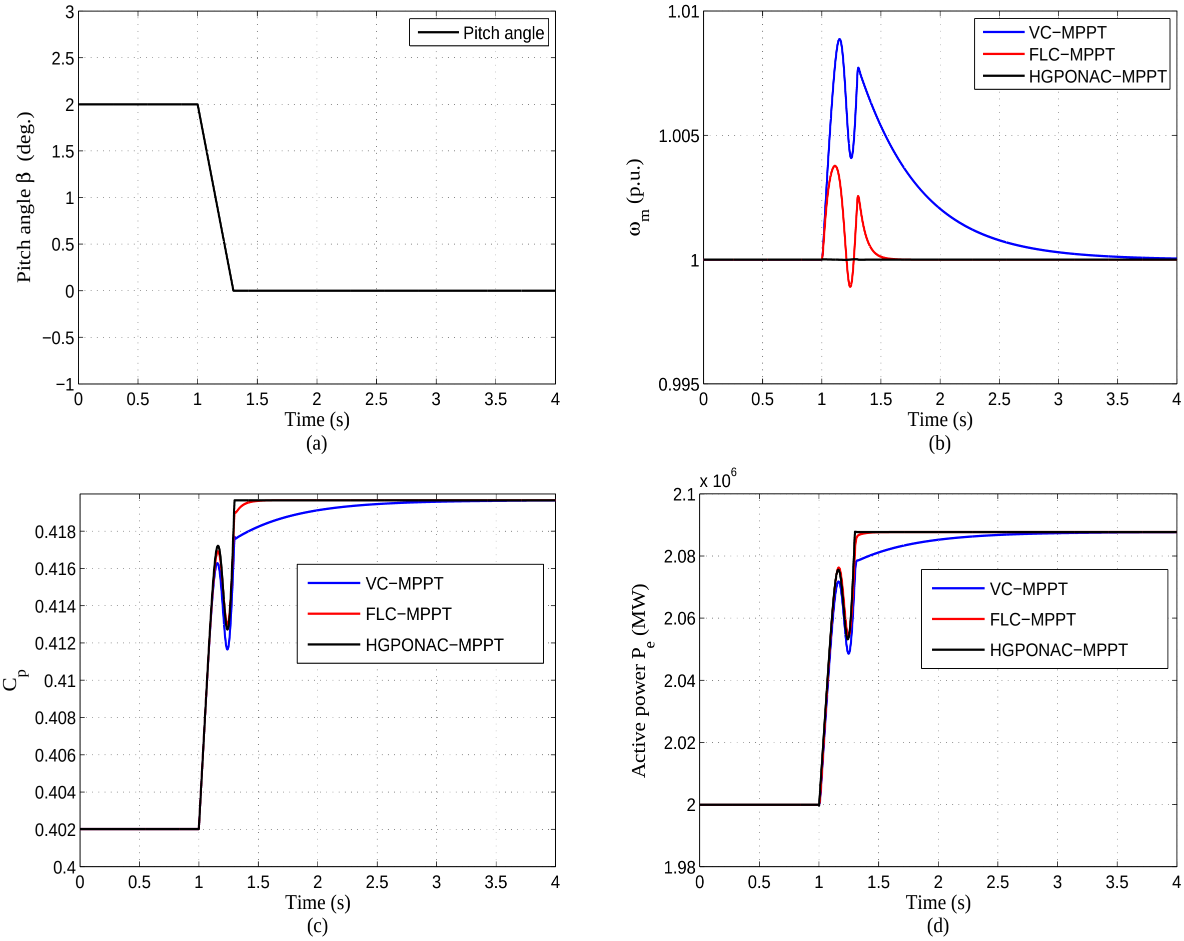

Figure 12: Responses obtained under pitch angle variation. (a) Pitch angle; (b) Mechanical rotation speed; (c) Power coefficient; and (d) Active power.

5. Experimental Validation

In this section, a simple experimental test is studied to show the performance of the proposed HGPONAC-MPPT. As mentioned in previous section, the FLC-MPPT requires accurate system parameters to test its performance. However, some parameters of the motor used in the experiment setup are not completely in accordance with the ones given on motor nameplate. Therefore, the comparison between the traditional VC-MPPT and the proposed HGPONAC-MPPT is given in this section. Moreover, it is not easy to simulate the operation conditions under parameter uncertainties and under tower shadow, therefore, only the operation under time-varying wind speed is tested.

Table 3: Parameters of PMSG-WT for experimental study

Parameters	Values	Units
Blade radius R	0.671	m
Air density ρ	1.205	kg/m^3
Rated wind speed V_r	9	m/s
Rated output power P_g	250	W
Stator resistance R_s	0.19	$\mu\Omega$
inductance in d-axis L_d	0.00049	H
inductance in q-axis L_q	0.00049	H
Number of pole pairs p	5	
Field flux K_e	0.0151	$V \cdot s/rad$
Total inertia J	1.23×10^{-3}	$kg \cdot m^2$

5.1. Experimental platform

The experimental setup depicted in Fig. 13 consists of a PMSG bench, a power electronic converter unit, a DS1104 controller with interface board, MATLAB/Simulink and dSPACE control desk. The PMSG bench includes a DC motor and a PMSG, in which the DC motor is used to emulate wind turbine. The controlled DC motor is usually used to emulate the behaviour of a wind turbine [15, 49, 50, 51, 52]. In this paper, the wind turbine is emulated using a DC motor with torque control. In the prototype, a 250 W, 4000 r/min DC motor was used. The wind turbine torque is calculated through wind input file and taking into account wind turbine rotational speed, wind

Table 4: Parameters of MPPT control schemes for simulation study

Parameters of the HGPONAC-MPPT (40)		
Gains of observer (34)	(20)	$pole = 100, \alpha_{11} = 2 \times 100 = 200, \alpha_{12} = 100^2$
	(19)	$\epsilon_1 = 0.05, l_{11} = \frac{\alpha_{11}}{\epsilon_1} = 4 \times 10^3, l_{12} = \frac{\alpha_{12}}{\epsilon_1^2} = 4 \times 10^6$
Gains of observer (35)	(20)	$pole = 160, \alpha_{21} = 3 \times 160 = 480, \alpha_{22} = 3 \times 160^2 = 7.68 \times 10^4,$ $\alpha_{23} = 160^3 = 4.096 \times 10^6$
	(19)	$\epsilon_2 = 0.05, l_{21} = \frac{\alpha_{21}}{\epsilon_2} = 9.6 \times 10^3, l_{22} = \frac{\alpha_{22}}{\epsilon_2^2} = 3.072 \times 10^7, l_{23} = \frac{\alpha_{23}}{\epsilon_2^3} = 3.2768 \times 10^{10}$
Gains of linear controller (37)	$k_{11} = 10, k_{21} = 256, k_{22} = 32$	

velocity, and wind turbine power coefficient curve (a lookup table in the computer was used). The obtained wind turbine torque is used as the torque reference of DC motor. The torque control is realized through the designed PI controller. The corresponding control system block diagram is depicted in Fig. 14. The parameters of the PMSG-WT are listed in Table 3. The control algorithms constructed in the Simulink platform are compiled to C-code via MATLAB/Simulink real-time workshop and then downloaded to the DS1104 dSPACE processor board, which in turn provides the PWM signal to control the IGBT-based electronic converter for driving the PMSG and the DC motor. The dSPACE processor board is also used to receive the mechanical speed and position measured by an incremental optical 1000-line encoder, which is synchronized with the motor shaft. The measured results of motor states are displayed on the dSPACE control desk, and both the reference control targets and the controller parameters can be adjusted in real time. The control parameters of the PONAC are given in Table 4. This paper mainly focuses on validating the effectiveness of the proposed control scheme through the emulated wind turbine experiment platform, which does not focus on wind turbine emulation. Therefore, the difference of power coefficient C_p function for different wind turbine is not considered in experimental validation. In this paper, the wind turbine is directly connected to the generator, which means that the gear ratio $n_{\mathrm{g}} = 1$. Therefore, the total inertia of the drive train shown in (8) equals to the summation of wind turbine inertia and generator inertia [2, 38]. In the test rig, a controlled DC motor is used to emulate the behaviour of a wind turbine and directly connected to the PMSG. Hence, the total inertia of the drive train equals to the summation of DC motor inertia and PMSG inertia at the test rig. It can be found from Figs. 15 and 17 that the desired emulator performance can be basically consistent with the practical wind turbine. In addition, since this paper mainly focuses on validating the effectiveness of the proposed robust MPPT controller for grid-connected PMSG-based wind turbine via the emulated rig test, the emulator performance in this paper is enough for this purpose.

5.2. Operation under ramp-change wind

The responses of the PMSG-WT to ramp-change wind are shown in Fig. 15. It can be found from Fig. 15 (b) and (c) that the proposed HGPONAC-MPPT can provide a satisfactory tracking performance of the mechanical rotation speed ω_{m} as wind speed varies. However, when the wind speed is fixed to be 2m/s after the great drop from 4m/s to 2m/s around 30s, the mechanical rotation speed of the PMSG-WT equipped with the VC-MPPT still has small period drop, instead of quickly switching to its optimal value, and the maximum tracking error reaches approximately 25%. Hence, the power coefficient C_p cannot always maintain at maximum value under VC-MPPT, shown in Fig. 15 (d). The main reason is that in the experiment test, the VC-MPPT is not only affected by the change of wind speed, but

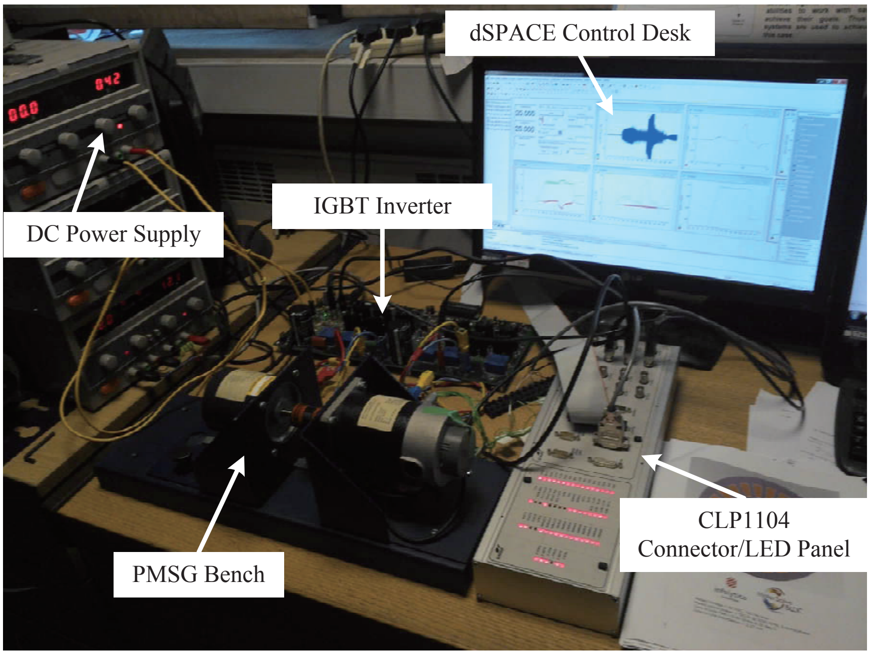

Figure 13: Experimental platform

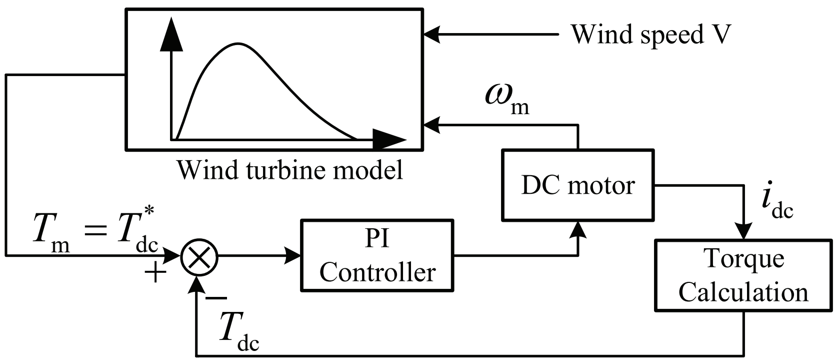

Figure 14: Control system of wind turbine emulator

also the system parameter uncertainties and unknown disturbances will further affect the controller performance. As mentioned in previous section, the main advantage of the proposed HGPONAC-MPPT is achieved by estimating the defined perturbation terms, (28) and (29), through the perturbation observers. The real value of perturbations and the estimated value provided by observers are compared in Fig. 16, in which the results show that the observers provide great estimations. When the observation error is within a certain range, the performance of the proposed controller can achieve satisfactory performances. It can be seen from Fig. 15 that, the mechanical rotation speed can be well

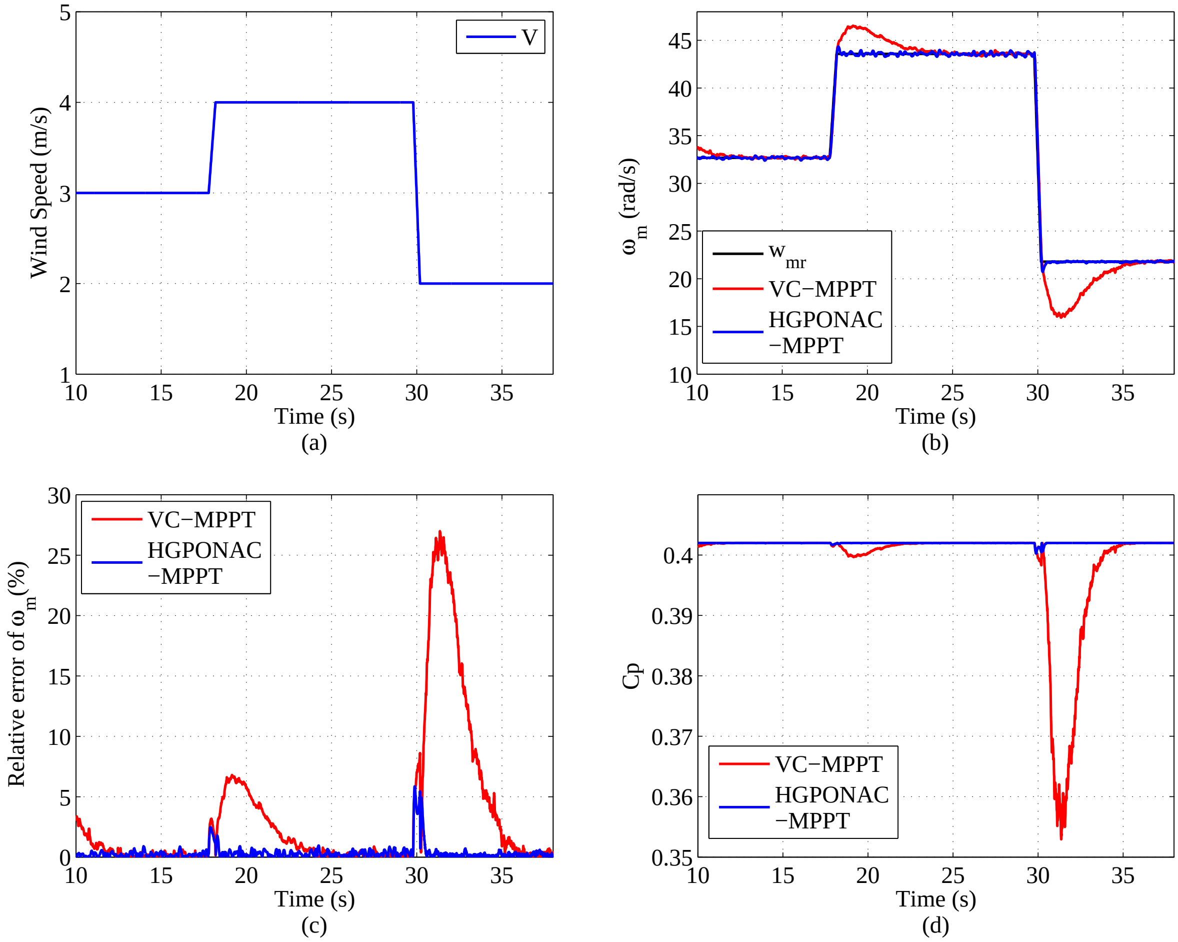

Figure 15: Responses for the case of ramp-change wind. (a) Wind speed V; (b) Mechanical rotation speed ω_{m}; (c) Relative error of mechanical rotation speed ω_{m}; and (d) Power coefficient C_p.

tracked and maximum wind power can be extracted from wind under the proposed HGPONAC-MPPT.

5.3. Operation under random wind

The responses of the PMSG-WT to random wind are shown in Fig. 17. It is obvious that the HGPONAC-MPPT provides better performance compared with the VC-MPPT. With the change of wind speed, the mechanical rotation speed of the PMSG equipped with the HGPONAC-MPPT can be well tracked with an acceptable error (smaller than 5% for most cases, shown in Fig. 17 (c)), which further makes the PMSG-WT work in a highly effective condition ($C_p > 0.4$ for most cases, shown in Fig. 17 (d)). However, for the one with the VC-MPPT, the mechanical rotation speed cannot quickly switch to its optimal value after the great wind speed drop (For example, around 25s).

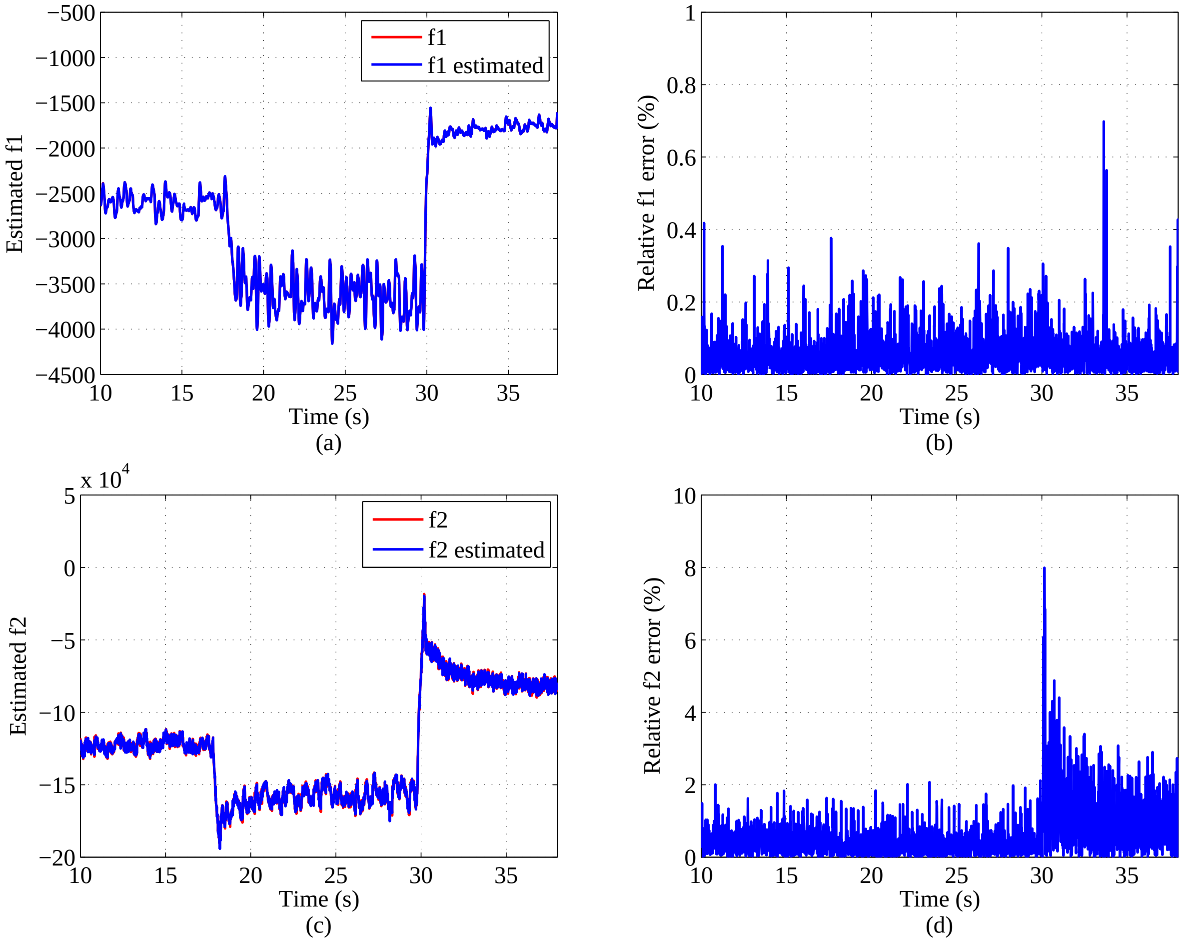

Figure 16: Estimates of perturbations

It can be seen from Figs. 15 and 17 that the mechanical rotation speed ω_{m} can keep at its optimal reference ω_{mr}. According to (9), the optimal T_{m} can be provided by the wind turbine, which means the DC motor can provide the expected torque for the PMSG under PI control.

5.4. Error analysis

For the error analysis of the experiments, the difference of the results obtained from the experiments compared with that of the simulation are mainly listed in the following four aspects,

- Measurement disturbances unavoidably exist in the experiment test. However, these disturbances has not taken into account in the simulation.

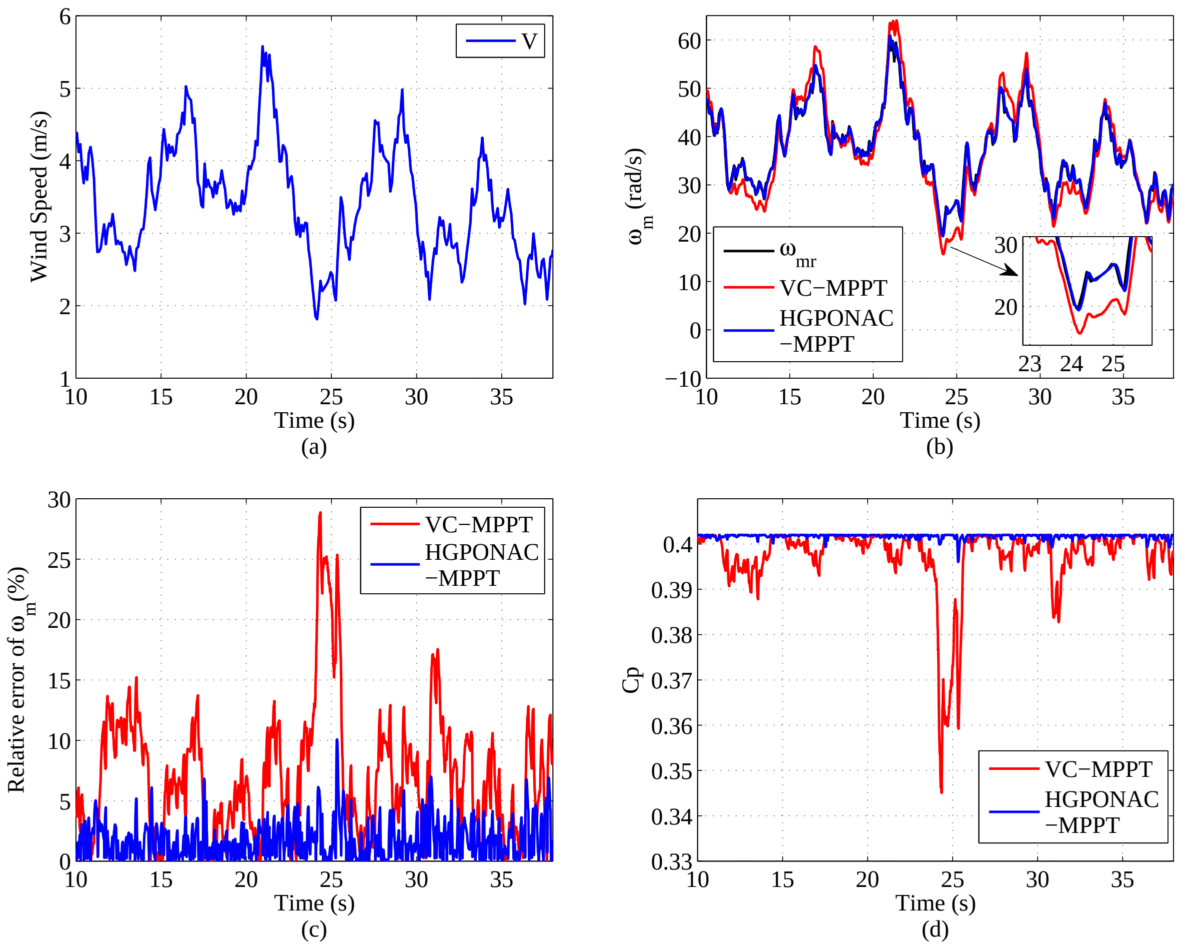

Figure 17: Responses for the case of random wind. (a) Wind speed V; (b) Mechanical rotation speed ω_{m}; (c) Relative error of mechanical rotation speed ω_{m}; and (d) Power coefficient C_p.

- In the experiment test, the vector control is not only affected by the change of wind speed, but also the system parameter uncertainties. Moreover, unknown disturbances will further affect the controller performance.
- Compared with the continuous control used in the simulation, the discretization of controller in the experiments and sampling holding may introduce an additional amount of error.
- The real-time controller in the experiment test exists time delay, whose exact value is unlikely to obtain in practice. However, a time delay Ts = 2 ms is assumed in the simulation.

6. Conclusions

This paper proposes a HGPONAC-based MPPT control scheme for the PMSG-WT to improve the energy conversion efficiency. The HGPOs are designed to estimate the system states and a lumped perturbation, which includes all possibly unknown and time-varying dynamics of the PMSG-WT, such as parameter uncertainties and nonlinearities, and disturbances. Therefore, a nonlinear adaptive controller with the estimates of the HGPOs and a linear output feedback control law is applied to compensate the actual perturbation of the PMSG-WT and achieve the MPPT. Compared with the VC-MPPT tuned around a specific operation point, the HGPONAC-MPPT can provide global optimal performance across the whole operation region. Due to no requirement of accurate model and full-state measurements, the HGPONAC-MPPT has a relatively simpler controller and much better robustness than the VC-MPPT and model based FLC-MPPT. Both simulation studies and experimental tests are carried out for the comparison of the MPPT performance provided by the proposed HGPONAC-MPPT, the VC-MPPT, and the FLC-MPPT under different operation conditions. The results show that, compared with both the VC-MPPT and the FLC-MPPT, the proposed HGPONAC-MPPT can always provides the highest energy conversion efficiency and best robustness against the time-varying wind speed, parameter uncertainties, as well as other external disturbances like the effect of tower shadow. In addition, the control performance of the HGPONAC-MPPT is better than that of the other observer-based control schemes (SMPONAC-MPPT and ADRC-MPPT) in terms of the maximum regulation error and ITAE. In further work, wind speed sensorless control scheme will be developed, as the wind speed cannot always be precisely measured in reality and anemometers increase the total cost of the system. The effective wind speed can be estimated by using the wind turbine itself as a measurement device, which can be applied in optimal TSR control scheme or pitch angle control scheme. Meanwhile, control schemes like perturbation and observation control without knowing maximum power coefficient will also be included in future work.

Acknowledgments

This work was supported by the National Natural Science Foundation of China under Grant No. 51577075.

References

[1] Li HH, Chen Z. Overview of different wind generator systems and their comparisons, IET Renew. Power Gener. 2008; 2(2): 123-138.

[2] Yang B, Yu T, Shu HC, Zhang YM, Chen J, Sang YY, Jiang L. Passivity-based sliding-mode control design for optimal power extraction of a PMSG based variable speed wind turbine, Renewable Energy 2018; 119: 577-589.

[3] Liu J, Wen JY, Yao W, Long Y. Solution to short-term frequency response of wind farms by using energy storage systems. IET Renewable Power Gener. 2016; 10(5): 669-678.

[4] Ajami A, Alizadeh R, Elmi M. Design and control of a grid tied 6-switch converter for two independent low power wind energy resources based on PMSGs with MPPT capability, Renewable Energy 2016; 87: 532-543.

[5] Liao SW, Yao W, Han XN, Wen JY, Cheng SJ. Chronological operation simulation framework for regional power system under high penetration of renewable energy using meteorological data. Appl. Energy. 2017; 203: 816-828.

[6] Dash PK, Patnaik RK, Mishra SP. Adaptive fractional integral terminal sliding mode power control of UPFC in DFIG wind farm penetrated multimachine power system. Protection and Control of Modern Power Systems, 2018; 3(3): 79-92.

[7] Boubzizi S , Abid H, Elhajjaji A, Chaabane M. Comparative study of three types of controllers for DFIG in wind energy conversion system. Protection and Control of Modern Power Systems, 2018; 3(3): 214-225.

[8] Yang B, Jiang L, Wang L, Yao W, Wu QH. Nonlinear maximum power point tracking control and modal analysis of DFIG based wind turbine. Int. J. Electr. Power Energy Syst. 2016; 74: 429-436.

[9] Karakasis NE, Mademlis CA. High efficiency control strategy in a wind energy conversion system with doubly fed induction generator, Renewable Energy 2018; 125: 974-984.

[10] Fantino R, Solsona J, Busada C. Nonlinear observer-based control for PMSG wind turbine, Energy 2016; 113: 248-257.

[11] Errouissi R, Al-Durra A. A novel PI-type sliding surface for PMSG-based wind turbine with improved transient performance, IEEE Trans. Energy Convers. 2018, 33(2):834-844.

[12] Li S, Li J. Output Predictor-based active disturbance rejection control for a wind energy conversion system with PMSG, IEEE Access 2017, 5:5205-5214.

[13] Errami Y, Ouassaid M, Maaroufi M. A performance comparison of a nonlinear and a linear control for grid connected PMSG wind energy conversion system. Int. J. Electr. Power Energy Syst. 2015; 68: 180-194.

[14] Li SH, Haskew TA, Swatloski RP, Gathings W. Optimal and direct-current vector control of direct-driven PMSG wind turbines. IEEE Trans. Power Electron. 2012; 27(5): 2325-2337.

[15] Chinchilla M, Arnaltes S, Burgos JC. Control of permanent-magnet generators applied to variable-speed wind-energy systems connected to the grid. IEEE Trans. Energy Convers. 2006; 21(1): 130-135.

[16] Yan JH, Lin HY, Feng Y, Zhu ZQ. Control of a grid-connected direct-drive wind energy conversion system, Renewable Energy 2014; 66: 371-380.

[17] Xie D, Lu YP, Sun JB, Gu CH. Small signal stability analysis for different types of PMSGs connected to the grid, Renewable Energy 2017; 106: 149-164.

[18] Yang B, Zhang XS, Yu T, Shu HC, Fang ZH. Grouped grey wolf optimizer for maximum power point tracking of doubly-fed induction generator based wind turbine. Energy Convers. Manage. 2017; 133: 427-443.

[19] Yang B, Yu T, Shu HC, Dong J, Jiang L. Robust sliding-mode control of wind energy conversion systems for optimal power extraction via nonlinear perturbation observers. Appl. Energy. 2018; 210: 711-723.

[20] Shen Y, Yao W, Wen JY, He HB. Adaptive wide-area power oscillation damper design for photovoltaic plant considering delay compensation. IET Gener. Transm. Distrib. 2017; 11(18): 4511-4519.

[21] Abdullah MA, Yatim AHM, Tan WC, Saidur R. A review of maximum power point tracking algorithms for wind energy systems. Renewable

Sustainable Energy Rev. 2012; 16(5): 3220-3227.

[22] Liu J, Yao W, Fang JK, Wen JY, Cheng SJ. Stability analysis and energy storage-based solution of wind farm during low voltage ride through. Int. J. Electr. Power Energy Syst. 2018; 101: 75-84.

[23] Shen Y, Yao W, Wen JY, He HB, Chen WB. Adaptive supplementary damping control of VSC-HVDC for interarea oscillation using GrHDP. IEEE Trans. Power Syst.. 2018; 33(2): 1777-1789.

[24] Liu ZQ, Yao W, Wen JY, Cheng SJ. Effect analysis of generator governor system and its frequency mode on inter-area oscillations in power systems. Int. J. Electr. Power Energy Syst. 2018; 96: 1-10.

[25] Li SH, Haskew TA, Xu L. Conventional and novel control designs for direct driven PMSG wind turbines. Electr. Power Syst. Res. 2010; 80(3): 328-338.

[26] Munteanu I, Cutululis NA, Bratcu AI, Ceanga E. Optimization of variable speed wind power systems based on LQG approach. Control Eng. Pract. 2005; 13(7): 903-912.

[27] Chen J, Jiang L, Yao W, Wu QH. A feedback linearization control strategy for maximum power point tracking of a PMSG based wind turbine, In: 2th International conference on renewable energy research and applications (ICRERA13), Madrid, Spain; 79-84 October 2013.

[28] Mullane A, Lightbody G, Yacamini R. Wind-turbine fault ride-through ehancement. IEEE Trans. Power Syst. 2005; 20(14): 1929-1937.

[29] Jung J, Lim S. A feedback linearizing control scheme for a PWM converter-inverter having a very small dc-link capacitor. IEEE Trans. Ind. Appl. 1999; 35(5): 1124-1131.

[30] Rahman MA, Vilathgamuwa DM, Uddin MN, Tseng KJ. Nonlinear control of interior permanent-magnet synchronous motor. IEEE Trans. Ind. Appl. 2003; 39(2): 408-416.

[31] Kim KH, Jeung YC, Lee DC, Kim HJ. LVRT scheme of PMSG wind power systems based on feedback linearization. IEEE Trans. Power Electron. 2012; 27(5): 2376-2384.

[32] Baik IC, Kim KH, Youn MJ. Robust nonlinear speed control of PM synchronous motor using boundary layer integral sliding mode control technique. IEEE Trans. Control Syst. Technol. 2000; 8(1): 47-54.

[33] Xia CL, Geng Q, Gu X, Shi TN, Song ZF. Input-output feedback linearization and speed control of a surface permanent-magnet synchronous wind generator with the boost-chopper converter. IEEE Trans. Ind. Electron. 2012; 59(9): 3489-3500.

[34] Yoo A, Sul SK. Design of flux observer robust to interior permanent-magnet synchronous motor flux variation. IEEE Trans. Ind. Appl. 2009; 45(5): 1670-1677.

[35] Mauricio JM, Leon AE, Gomez-Exposito A, Solsona JA. An adaptive nonlinear controller for DFIM-based wind energy conversion systems. IEEE Trans. Energy Convers. 2008; 23(4): 1025-1035.

[36] Jiang L, Wu QH, Wen JY. Decentralized nonlinear adaptive control for multimachine power systems via high-gain perturbation observer. IEEE Trans. Circuits Syst. Regul. Pap. 2004; 51(10): 2052-2059.

[37] Chen J, Jiang L, Yao W, Wu QH. Perturbation estimation based nonlinear adaptive control of a full-rated converter wind-turbine for fault ride-through capability enhancement. IEEE Trans. Power Syst. 2014; 29(6): 2733-2743.

[38] Uehara A, Pratap A, Goya T, Senjyu T, Yona A, Urasaki N, Funabashi T. A coordinated control method to Smooth wind power fluctuations of a PMSG-based WECS. IEEE Trans. Energy Convers. 2011; 26(2): 550-558.

[39] Tan K, Islam S. Optimum control strategies in energy conversion of PMSG wind turbine system without mechanical sensors. IEEE Trans. Energy Convers. 2004; 19(2): 392-399.

[40] Jaramillo-Lopez F, Kenne G, Lamnabhi-Lagarrigue F. A novel online training neural network-based algorithm for wind speed estimation and adaptive control of PMSG wind turbine system for maximum power extraction, Renewable Energy 2016; 86: 38-48.

[41] Johnson KE, Pao LY, Balas MJ, Finfersh LJ. Control of variable-speed wind turbines: standard and adaptive techniques for maximizing energy capture. IEEE Control Syst. Mag. 2006; 26(3): 70-81.

[42] Asghar AB, Liu XD, Estimation of wind turbine power coefficient by adaptive neuro-fuzzy methodology. Neurocomputing. 2017; 238:227-233.

[43] Petkovic D, Cojbasic Z, Nikolic V, Adaptive neuro-fuzzy approach for wind turbine power coefficient estimation. Renewable Sustainable Energy Rev. 2013; 28:191-195.

[44] Dai JC, Liu DS, Wen, Long X. Research on power coefficient of wind turbines based on SCADA data. Renewable Energy 2016; 86:206-215.

[45] Jiang L, Nonlinear adaptive control and applications in power systems, Ph.D. thesis, University of Liverpool, UK.

[46] Jiang L, Wu QH. Nonlinear adaptive control via sliding-mode state and perturbation observer. IEE Proc. Inst. Electr. Eng.-Control Theory Appl., 2002; 149(4): 269-277.

[47] Han JQ. From PID to active disturbance rejection control, IEEE Trans. Ind. Electron.2009; 56(3): 900-906.

[48] Dolan DSL, Lehn PW. Simulation model of wind turbine 3p torque oscillations due to wind shear and tower shadow. IEEE Trans. Energy Convers. 2006; 21(3): 717-724.

[49] Rabelo B, Hofmann W, Gluck M. Emulation of the static and dynamic behaviour of a wind-turbine with a DC-machine drive. IEEE Power Electronics Specialists Conference 2004; 3: 2107C2112.

[50] Abdeddaim S, Betka A, Drid S, Becherif M. Implementation of MRAC controller of a DFIG based variable speed grid connected wind turbine. Energy Convers. Manage. 2014; 79: 281-288.

[51] Roberto R, Pena R, Tobar G, Clare J, Wheeler P, Asher G. Stability analysis of a wind energy conversion system based on a doubly fed induction generator fed by a matrix converter. IEEE Trans. Ind. Electron. 2009; 56(10): 4194-4206.

[52] Wei C, Zhang Z, Qiao W, Qu LY. Reinforcement-learning-based intelligent maximum power point tracking control for wind energy conversion systems. IEEE Trans. Ind. Electron. 2015; 62(10): 6360-6370.